

1 **On the Nationwide Variability of Low-Level Jets Prior**
2 **to Warm-season Nocturnal Rainfall in China Revealed**
3 **by Radar Wind Profilers**

4 Ning Li^{a,b,c}, Jianping Guo^{a,d*}, Xiaoran Guo^{a,d}, Tianmeng Chen^{a,d}, Zhen Zhang^a, Na
5 Tang^a, Yifei Wang^a, Honglong Yang^d, Yongguang Zheng^c, Yongshui Zhou^e

6 ^a *State Key Laboratory of Severe Weather Meteorological Science and Technology &*
7 *Specialized Meteorological Support Technology Research Center, Chinese Academy*
8 *of Meteorological Sciences, Beijing 100081, China*

9 ^b *College of Earth and Planetary Sciences, University of Chinese Academy of*
10 *Sciences, Beijing 100049, China*

11 ^c *National Meteorological Centre, Beijing 100081, China*

12 ^d *CMA Field Scientific Experiment Base for Low-Altitude Economy Meteorological*
13 *Support of Unmanned Aviation in Guangdong-Hong Kong-Macao Greater Bay Area,*
14 *Shenzhen 518108, China*

15 ^e *Guizhou Meteorological Observatory, Guiyang, China*

16
17
18
19
20 Correspondence to:

21 Dr./Prof. Jianping Guo (Email: jpguocams@gmail.com)
22

Deleted: ¶

Deleted: ¶

Deleted:

Field Code Changed

26
27
28
29
30
31
32
33
34
35
36
37
38
39
40
41
42
43
44
45
46
47
48
49

Abstract

Nocturnal rainfall initiation is closely linked to low-level jets (LLJs), but national-scale LLJ features over China—especially their evolution preceding warm-season nocturnal rainfall—remain unknown due to scarce high-resolution vertical wind observations. Here, we reveal the fine vertical structure of LLJs and their rapid evolution, within 2 hours preceding the onset of nocturnal heavy rain (HR) and non-HR across four phases of rainy seasons in China during the warm season (April–October) of 2023–2024, utilizing data from a nationwide network of radar wind profilers (RWPs) in combination with surface observations and reanalysis data. Results show that nocturnal rainfall accounted for over 50% of warm-season rainfall, with 56% preceded by LLJs within 2 hours leading up to their onset. In monsoon regions, approximately 45% of nocturnal HR were LLJ-associated (LLJ HR) and produced heavier rainfall than non-LLJ HR events. Critically, LLJ HR events underwent a minute-scale ‘rapid reorganization’ of LLJs structure, characterized by oscillatory evolution in jet height, frequency and strength. This creates favorable environment for the ‘final-stage intensification’ of dynamic field during the last ~30 min, where the widespread intensification of jet—coupled with significant thermodynamic instability—serves as a decisive triggering mechanism for HR. In stark contrast, LLJ non-HR events exhibit quasi-steady or weakening dynamical trends, accompanied by an inadequate thermodynamic response that lacks such synergistic coupling. These findings demonstrate that minute-scale dynamic adjustments, driven by swift evolution of the LLJ is essential for nocturnal HR, thereby providing observational constraints for regional model parameterizations and nowcasting accuracy.

- Deleted: multiscale responses of LLJs...within 2 hours preceding the onset of nocturnal heavy rain (HR) and non-HR across four phases of rainy seasons in China during the warm season (April-- ... [1]
- Formatted: English (US)
- Deleted: ~
- Deleted: had
- Deleted: exhibit
- Deleted: higher ...eavy ... [2]
- Formatted: Font color: Auto, Complex Script Font: Bold
- Deleted: probability
- Formatted: Font color: Auto, Complex Script Font: Bold
- Deleted: we identify a distinct two-stage evolutionary mechanism governing HR initiation. In the preparatory phase (30–120 min prior),
- Deleted: goed
- Formatted ... [3]
- Deleted: ...oscillatory evolutionoscillations ... [4]
- Deleted: prepare... favorable the ... [5]
- Deleted: with
- Deleted: in thearound
- Deleted: a universal...intensification of jet—...coupled ... [6]
- Formatted: English (US)
- Deleted: acts as the robust trigger for HR
- Deleted: sharp...contrast, LLJ_non-HR events exhibit ... [8]
- Formatted: Font color: Auto, English (US)
- Formatted ... [7]
- Deleted: and ...n inadequate thermodynamic respony ... [10]
- Formatted ... [9]
- Deleted: ing
- Deleted: this
- Deleted: This behavior stood in sharp contrast to LLJ ... [13]
- Formatted ... [11]
- Formatted ... [12]
- Deleted: a
- Deleted: 'rapid reorganization...ynamic adjustments'. ... [14]
- Formatted ... [15]

124
125
126
127
128
129
130
131
132
133
134
135
136
137
138
139

Short Summary

Nighttime rainfall often links to low-level jets (LLJs), but we lack clarity on nationwide LLJ features. We here used a nationwide radar wind profiler network to study LLJ changes 2 hours before rainfall, covering China's 2023–2024 rainy seasons. 56% nighttime rainfall had LLJs. The LLJs-associated heavy rain needed a rapid adjustment of LLJs' vertical structure, especially a significant intensification within 30 minutes preceding rain. This shows the importance of LLJ in nowcasting rainfall.

- Formatted: Font: Not Bold
- Formatted: Font color: Auto, Complex Script Font: Bold
- Deleted: due to limited wind data
- Deleted: To address this,
- Deleted: w
- Formatted: Font color: Auto, Complex Script Font: Bold
- Deleted: The heavy rains linked to LLJs
- Deleted: LLJs
- Formatted: English (US)
- Deleted: to strengthen quickly 30–120 minutes
- Deleted: These findings
- Deleted: nighttime
- Formatted: Font color: Auto, Complex Script Font: Bold
- Formatted: Font color: Auto, Complex Script Font: Bold
- Formatted: Font color: Auto, Complex Script Font: Bold, English (US)
- Formatted: Font color: Auto, Complex Script Font: Bold
- Formatted: Font color: Auto, Complex Script Font: Bold, English (US)
- Formatted: Font color: Auto, Complex Script Font: Bold

1. Introduction

Forecasting nocturnal heavy rainfall (HR) and associated severe convective weather remains a major challenge in hazardous weather prediction (Davis et al., 2003; Trier et al., 2006), owing to the complexity of triggering mechanisms, the scarcity of continuous high-resolution observations, and inaccuracies in model parameterizations (Carbone and Tuttle, 2008; Reif and Bluestein, 2017; Weckwerth et al., 2019; Zhao et al., 2025). Crucially, the low-level jet (LLJ) that exhibit a diurnal cycle with a maximum at night is widely recognized as a key contributor to nocturnal HR (Bonner 1968; Mitchell et al., 1995; Tuttle and Davis, 2006), as documented in regions or countries such as the Great Plains of the United States (Maddox, 1983; Higgins et al., 1997), Argentina (Marengo et al., 2004), India (Monaghan et al., 2010), North China Plain (Li et al., 2024).

The LLJs primarily originate from the inertial oscillations (IO) following the sudden decay of turbulence after sunset (Blackadar, 1957) and thermal imbalances induced baroclinicity over sloping terrain (Holton, 1967). Functioning as concentrated corridors for heat, moisture, and momentum transport, LLJs can modulate the diurnal oscillation in water vapor by IO (Rasmusson, 1967; Zhang et al., 2019) and enhance convective instability, particularly when elevated high- θ_e air encounters frontal boundaries (Trier et al., 2017). Also, strong low-level vertical wind shear (VWS) associated with LLJs necessarily benefits deep lifting (Maddox et al., 1979; Stensrud, 1996; Rasmussen and Houze, 2016). These mechanisms collectively provide essential thermodynamic and dynamic support for the initiation and organization of nocturnal convection, especially where LLJs force low-level ascent at jet termini or via positive vorticity advection left of the jet axis (Chen et al., 2017; Du and Chen, 2019; Xia and Zhao, 2009).

Furthermore, LLJs interact synergistically with other key factors to trigger HR that is associated with mesoscale convective systems (Chen et al. 2010; Chen et al., 2017; Chen et al., 2024), including terrain effects (Anthes et al., 1982; Pan and Chen, 2019; Huang et al., 2020), gravity waves (Weckwerth & Wakimoto, 1992), among others.

Formatted: Font: Bold, Complex Script Font: Not Bold

Formatted: Indent: First line: 0 ch

Deleted: and mesoscale convective systemsmesoscale systems (Chen et al. 2010; Chen et al., 2017; Chen et al., 2024), ...

180 These interactions are highly sensitive to the prevailing synoptic and subsynoptic-scale
181 environmental conditions (e.g., Hodges and Pu, 2019) and fine-scale structural of LLJs,
182 including LLJ frequency, spatial redistribution, and particularly localized wind profile
183 accelerations (Pitchford and London, 1962; Walters and Winkler, 2008; Du and Chen,
184 2019; Li et al., 2024). Understanding these intricate evolution features of LLJs is critical
185 for improving the forecasting of nocturnal HR.

186 Despite advances facilitated by regional reanalysis (e.g., Doubler et al., 2015; Li
187 et al., 2021), numerical modeling (e.g., Zhang and Meng, 2019), radiosonde
188 observations (e.g., Whiteman et al., 1997; Yan et al., 2020), and emerging artificial
189 intelligence techniques (e.g., Subrahmanyam et al., 2024) in understanding the
190 climatology and physical mechanisms of LLJs and their role in HR forecasting,
191 significant knowledge gaps remain. **A** critical shortcoming lies in the inability to
192 capture minute-scale evolution of LLJs during the nocturnal pre-storm period.
193 Conventional observing systems lack the spatiotemporal resolution required to resolve
194 rapid changes in pre-storm environments (Weisman et al., 2015; Cao et al., 2025; Roots
195 et al., 2025), thereby hindering systematic analysis of fine-scale structure of LLJs and
196 their evolution within the critical 2-hour window preceding rainfall.

197 Moreover, the mechanisms and impacts of LLJs exhibit considerable variation
198 across monsoon phases and geographic regions. As a classic monsoon climate region,
199 China exhibits particularly prominent nocturnal rainfall contributions across major
200 climate-sensitive areas (Yu et al., 2014), where LLJs play a crucial role in modulating
201 primary rainfall belts (Sun, 1986; Chen et al., 2010; Wang et al., 2013; Horinouchi et
202 al., 2019), such as those in Eastern China (Chen et al., 2017; Xue et al., 2018) and South
203 China (Du et al., 2020; Bai et al., 2021; Fu et al., 2021). However, nationwide
204 comparative studies examining LLJ precursor signals across different monsoon phases
205 in China are still lacking.

206 **R**adar wind profilers (RWPs) can offer transformative potential by capturing
207 minute-resolution wind profiles to reveal pre-rainfall dynamic precursors (Zamora et
208 al., 1987; Du et al., 2012; Molod et al., 2019; Guo et al., 2023). For example, Gebauer

Deleted: However, a

Formatted: Font color: Auto, Complex Script Font: Bold

210 et al. (2018) demonstrated the capability of RWPs to elucidate how heterogeneous
211 structures of LLJ trigger nocturnal convection in Great Plains; Based on a linear net of
212 RWPs deployed across the North China Plain, our previous study (Li et al., 2024)
213 observed rapid intensification of moisture flux convergence (MFC) driven by a surge
214 in LLJs profile within 30 min preceding nocturnal rainfall onset, highlighting the
215 sensitivity of RWP to minute-scale perturbations of LLJs profiles. However, it remains
216 an open question whether this minute-scale precursor is universally applicable across
217 diverse monsoon phases throughout mainland China. Furthermore, the systematic
218 differences in the fine-scale LLJ evolution that distinguish HR from non-HR have yet
219 to be fully elucidated.

220 Therefore, this study utilizes a nationwide network of RWPs to address the
221 following two questions: 1) How do the vertical structure of LLJs and their minute-
222 scale evolution within 0–2 hours preceding nocturnal rainfall vary across different rainy
223 season phases? and 2) What are the systematic differences in LLJ dynamic-
224 thermodynamic mechanisms between LLJ-influenced HR and non-HR events? The
225 remainder of this paper is structured as follows: Section 2 details data and methodology,
226 Section 3 presents comparative analyses of characteristics of rainfall and LLJs
227 evolution, and Section 4 synthesizes key conclusions.

228

229 **2. Data and Methodology**

230 *2.1 Radar wind profiler measurements*

231 The RWP observations collected from 31 stations across China (Fig.1) from April
232 to October in 2023–2024 were analyzed in this study, which can provide wind speed
233 and direction with a vertical resolution of 120 m and an interval of 6 minutes (Liu et al.,
234 2019). To reduce the potential influence of poor data quality, RWP data underwent
235 strict quality control following procedures proposed by Wei et al. (2014) and Miao et
236 al. (2018). Firstly, to minimize contamination from precipitation particles, which can
237 introduce significant errors in Doppler-based wind retrieval, all observations during

Deleted: (

Deleted: across China

Deleted: '

Deleted: s

Deleted: ing

Deleted: heavy

Deleted: heavy rainfall events

Formatted: Font color: Auto, Complex Script Font: Bold

Formatted: Font color: Auto, Complex Script Font: Not Bold

Formatted: Font color: Auto, Complex Script Font: Bold

Deleted: -

Formatted: English (US)

246 ~~rainfall periods were removed.~~ Secondly, within each profile below 3 km above ground
247 ~~level (AGL),~~ missing values and significant outliers that defined as values exceeding
248 2.5 standard deviations from the mean were removed. ~~Next, for each profile, if more~~
249 ~~than 40% of the data points below 3 km AGL were outliers or missing, that entire profile~~
250 ~~was discarded.~~ Finally, discontinuous, or missing data points were estimated using
251 linear interpolation. Following this quality control process, 109,400 wind profiles were
252 discarded and a total of 2,606,042 profiles across China were available for analysis
253 during the study period.

Deleted: observations recorded during rainfall periods were eliminated because RWPs are susceptible to contamination by precipitation particles.

Deleted: for each profile, if more than 40% of the data points below 3 km above ground level (AGL) were outliers or missing, that entire profile was discarded. Next,

254 ~~2.2 Multi-source meteorological data~~

Deleted: Miscellaneous

Formatted: Font color: Auto, Complex Script Font: Bold

255 In addition, 1-min rainfall measurements were directly acquired from the rain
256 gauge measurements at 2160 national weather stations across China to identify rainfall
257 events. Rainfall amounts were accumulated over 6-min intervals to ensure temporal
258 alignment with the RWP measurements. Ground-based meteorological variables are
259 measured at 1-min intervals from national weather stations, including 2-m air
260 temperature, relative humidity, and surface pressure. All ground-based data have
261 undergone rigorous quality control (~~China Meteorological Administration, 2020; Zhao~~
262 ~~et al., 2024)~~ and are publicly ~~accessible at the National Meteorological Information~~
263 ~~Center of China Meteorological Administration (CMA).~~

Deleted: available

Deleted: by

Deleted: China

Deleted: Administration (CMA)

264 Furthermore, to diagnose large-scale circulation patterns and environmental
265 conditions preceding nocturnal rainfall influenced by LLJs, this study utilized
266 meteorological variables derived from the fifth generation of the European Centre for
267 Medium-Range Weather Forecasts atmospheric reanalysis (ERA5) of the global
268 climate (Hersbach et al., 2020). The ERA5 data features a horizontal resolution of
269 0.25°×0.25° across 37 vertical pressure levels and hourly temporal resolution. Unless
270 otherwise specified, all datasets cover the study period of April to October in 2023–
271 2024.

283 **2.3 Identification of nocturnal rainfall events**

Formatted: Font color: Auto, Complex Script Font: Bold

284 Firstly, days with typhoon activity were excluded. To minimize the impact of
285 rainfall on RWP measurements, a minimum dry interval of 2 hours was required
286 between consecutive rainfall events. Following the methodology of Li et al. (2024), a
287 rainfall occurrence was defined when the total accumulated rainfall which was
288 measured by all rain gauges within a 25-km radius of each RWP station exceeded 0.1
289 mm. Accounting for rainfall intermittency, a valid rainfall event required at least two
290 subsequent occurrences within 30 min following initial detection. Any isolated initial
291 occurrence not meeting this criterion was discarded. Notably, this 25-km radius serves
292 as a rigorous spatial constraint to not only mitigates the limitations of single-gauge
293 measurements but also ensures the onset of rainfall at this scale are temporally coherent
294 with that of the rain gauge co-located with RWP (as confirmed by sensitivity tests in
295 Fig. S1). This guarantees direct physical coupling between local rainfall and the RWP-
296 observed wind profiles.

Formatted: English (US)

Formatted: English (US)

Deleted: Notably, this radius was selected as a rigorous spatial constraint to ensure a tight physical coupling between the local rainfall and the precursor wind profile detected by the RWP. Consequently, this study focuses strictly on 'overhead' LLJs co-located with rainfall to guarantee the physical validity of the analyzed fine-scale dynamic-thermodynamic relationships, although this conservative criterion excludes cases influenced by upstream jets.

297 Nocturnal rainfall events were defined as those occurring between 2000 and 0800
298 Local Standard Time (LST). Based on operational classifications from the National
299 Water Resources Bureau and CMA, the rainy season was categorized into four
300 consecutive phases: (1) the South China Pre-summer Rainy Season (April 1 to June 8,
301 2023 and April 1 to June 9, 2024), (2) the Meiyu Season (June 9 to July 14, 2023 and
302 June 10 to July 21, 2024), (3) the North China Rainy Season (July 15 to August 31,
303 2023 and July 22 to August 31, 2024), and (4) the West China Autumn Rainy Season
304 (September 1 to October 31 for both 2023 and 2024). These phases are subsequently
305 designated as Phase 1 to Phase 4 throughout this study. Four regions of interest (ROIs)
306 were subsequently selected for detailed analysis (see Table 1).

Deleted: 22

Deleted: 15

Deleted: ,

Deleted:

Formatted: First line: 2 ch, Space Before: 0 pt, After: 0 pt

307 Further screening identified locally nocturnal HR events, where the mean 6-min
308 rainfall intensity exceeded the 75th percentile of all recorded rainfall events at each
309 station. This threshold can effectively distinguish significant HR from weak rainfall
310 while ensuring a sufficient sample size for robust statistical analysis of minute-scale
311 LLJ dynamics (Table S1). Furthermore, a sensitivity test by varying the thresholds to

Deleted: This relative threshold was selected to accommodate the significant climatic heterogeneity across the nationwide domain, ensuring the identification of locally significant HR events in both arid and humid regions (Zhai et al., 2005; Zhang and Zhai, 2011).

Formatted: Font color: Auto, Complex Script Font: Bold

Formatted: Font: (Asian) SimSun, Font color: Auto, Complex Script Font: Bold, English (US)

329 85th and 95th percentile to ensure that the main conclusion regarding the precursory
330 signals of LLJs is robust within a reasonable threshold range (see Figs. S2–S5).

331 Statistical analysis revealed 3,155 nocturnal rainfall events during the 2023–2024
332 warm seasons (within the 31 red circles shown in Fig.1). Event counts per rainy season
333 phase were 1,109, 689, 652, and 705 respectively, with 841 events classified as
334 nocturnal HR events.

335 2.4 Identification of LLJs and associated rainfall event

336 To ensure identified LLJs exhibit significant vertical wind shear characteristic of
337 jet-like profiles, the following criteria are adopted: (1) a maximum horizontal wind
338 speed exceeding 10 m s^{-1} in the lowest 3 km AGL, and (2) a wind speed reduction of
339 at least 3 m s^{-1} from the maximum to minimum below 3 km AGL, or to 3 km AGL if
340 no minimum exists. These deliberately conservative wind speed thresholds maximize
341 LLJ sample size for enhanced statistical robustness. This definition standard has been
342 widely adopted in previous studies (Bonner, 1968; Whiteman et al., 1997; Du et al.,
343 2014; Yan et al., 2020). The strength of LLJ or jet nose is defined as the maximum wind
344 speed along the entire profile. The LLJ core height is defined as the altitude of the wind
345 speed maximum during LLJ occurrences. Correspondingly, the LLJ direction is
346 determined by the wind direction at the height of the LLJ.

347 We define rainfall events where LLJ occurs at least twice within 2 hours before
348 rainfall as an LLJ event (Li et al., 2024). The HR events influenced by LLJs (LLJ_HR
349 events), HR events without LLJ influence (non-LLJ_HR events), and non-HR events
350 affected by LLJ (LLJ_non-HR events) are further distinguished.

352 3. Results and discussion

353 3.1 General characteristics of nocturnal rainfall and LLJs

354 Firstly, we characterized the spatiotemporal patterns of rainfall and LLJs observed
355 nationwide during the 2023–2024 warm season. Nationally, nocturnal rainfall
356 accounted for 50.9% of total warm-season rainfall, with pronounced concentrations

Deleted: sensitivity tests confirmed

Formatted: Font: (Asian) SimSun, Font color: Auto, Complex Script Font: Bold

Formatted: Font: (Asian) SimSun, Font color: Auto, Complex Script Font: Bold, English (US)

Formatted: Font color: Auto, Complex Script Font: Bold

Deleted: this threshold can effectively distinguish significant HR from weak precipitation while ensuring a sufficient sample size for robust statistical analysis analysis of minute-scale LLJ dynamics. Supplementary analyses using a stricter 85th and 95th percentile threshold yielded consistent dynamical patterns (see Figs. S1 and S2 and Table S1), demonstrating that the identified precursor signals are physically robust.

Formatted: Not Highlight

Formatted: Not Highlight

Formatted: Font color: Auto, Complex Script Font: Bold

Deleted: (Bonner, 1968; Whiteman et al., 1997; Du et al., 2014; Yan et al., 2020).

Formatted: Font: (Default) Times New Roman, (Asian) SimSun, 12 pt, Complex Script Font: Times New Roman, 12 pt, Bold, English (US)

Formatted: Font: (Default) Times New Roman, (Asian) SimSun, 12 pt, Complex Script Font: Times New Roman, 12 pt, Bold, English (US)

Deleted: .

Deleted: And

Formatted: Font color: Auto, Complex Script Font: Not Bold

Formatted: Font color: Auto, Complex Script Font: Bold

Deleted: 1.6

Deleted: (Fig. 2g)

372 over North, Northeast and Southwest China (Figs. 2d and 2g). In contrast, the
373 pronounced daytime rainfall dominance in South China (Fig. 2a) may arise from the
374 interaction between enhanced onshore monsoonal flows and terrain (Bai et al., 2020),
375 sea breeze fronts and cold pool (Chen et al., 2016). In terms of frequency, nocturnal
376 rainfall occurred more frequent, constituting 52.5% of the total rainfall frequency
377 versus 47.5% for the daytime, with the highest nocturnal proportions found in
378 southwestern and eastern regions (Figs. 2e and 2h). Although the national mean rainfall
379 intensity was generally lower at night (1.2 mm/h) than during the day (1.2 mm/h; Figs.
380 2c and 2f), the probability of nocturnal HR occurrence was significant (51.3%),
381 particularly across western China, North China, and northeastern China (Fig. 2i).

382 Figure 3 displays the key attributes of LLJs detected at all 31 RWP across China
383 using the criteria defined in Section 2. Nocturnal LLJs activities occurred more
384 frequently, with an overall occurrence frequency increase of nearly 18% (Figs. 3a and
385 3e). Spatially, the regions exhibiting pronounced jet activity and high absolute wind
386 speeds were collocated with those experiencing intense nocturnal rainfall, particularly
387 over northern and eastern regions. Vertically, these jets manifest as intensified LLJ core
388 concentrated below 1 km AGL (Figs. 3f and 3g). This vertical restructuring likely
389 responds to nocturnal surface cooling and IO. The dominant wind direction shifted to
390 westerly, southerly or southwesterly flows at night across most regions, potentially
391 driven by thermal contrasts within the monsoon circulation pattern and topographic
392 forcing.

393 Statistical analysis revealed substantial linkage between LLJs and nocturnal
394 rainfall. Specifically, 56% of nocturnal rainfall events across China were preceded by
395 the presence of LLJs within 2 hours, establishing nocturnal rainfall influenced by LLJs
396 as a major component of warm-season rainfall in China. This relationship was
397 modulated by the seasonal migration of the western Pacific subtropical high (WPSH),
398 which drove corresponding shifts in HR belts that closely synchronized with the
399 spatiotemporal evolution of LLJ activity. The proportion of nocturnal rainfall events
400 associated with LLJs during the four rainy season phases reached 60.4%, 56.3%, 49.4%,

Formatted: Font: (Asian) SimSun, Complex Script Font: Bold, English (US)

Deleted: eastward propagation of rainfall (Jiang et al. 2017; Fu et al., 2021), the cloud top radiative cooling that enhances condensation and the intensified low-level convergence between onshore flows and land breezes (Bai et al., 2020)

Deleted: sea-breeze-front convective systems triggered by afternoon land-sea thermal contrasts and rapid destabilization of the local boundary layer.

Deleted: The relative contribution rate of frequency of The frequency of nocturnal rainfall (52.5%) notably exceeded that of daytime rainfall (47.5%)

Deleted: While the North China displayed distinct nocturnal

Deleted: nocturnal

Deleted: higher at night than during the day

Deleted: ¶

Deleted: ed

Formatted: Font color: Auto, Complex Script Font: Bold

Deleted: Section 2

Formatted ... [18]

Formatted: Font color: Auto, Complex Script Font: Bold

Formatted ... [19]

Formatted: Font color: Auto, Complex Script Font: Bold

Formatted ... [20]

Deleted: Compared to daytime, the occurrence frequency of nocturnal LLJs is higher

Deleted:

Deleted: where nocturnal rainfall is more intense.

Formatted ... [22]

Formatted ... [23]

Formatted ... [24]

Deleted: Nocturnal LLJs exhibited stronger strength of low-level wind-field modifications

Formatted: Font color: Auto, Complex Script Font: Bold

Deleted: resultant low-level wind-field modifications

Formatted: Font color: Auto, Complex Script Font: Bold

Deleted: .

Deleted: Consequently,

Deleted: represent

Deleted: And t

Formatted ... [26]

Formatted: Font color: Auto, Complex Script Font: Bold

438 and 54.9%, respectively (Fig. 4a). Among 841 identified nocturnal HR events, the
439 percentages classified as LLJ_HR events ranged from 33.9% to 47.2% across the four
440 phases. These results indicated that the mere presence of LLJs, while a frequent
441 precursor to general nocturnal rainfall, is necessary but insufficient for HR.

442 However, spatial analysis of site-averaged rainfall intensity revealed that LLJ HR
443 events consistently produced heavier rainfall than non-LLJ_HR events, particularly
444 within the four ROIs identified in each phase (red boxes in Fig. 5). The non-LLJ HR
445 events exhibited spatially heterogeneous intensity distributions, where localized
446 maxima may occur in areas outside the primary rain belts. For instance, during Phase 2
447 in ROI-3 (Fig. 5f), sporadic high-intensity events driven by deep cold trough system
448 resulted in high site-averaged intensities even without LLJs, whereas in ROI-2, the
449 absence of LLJs typically corresponded to weaker frontal precipitation (Fig. S6). This
450 reflected the dominant role of LLJ coupling in primary rain belts region. Furthermore,
451 a total of 71, 49, 33, and 34 nocturnal HR events were identified in these ROIs during
452 from Phase 1 to Phase 4 (Fig. 4b). From the LLJs perspective, nearly 31.1% of LLJ
453 events were classified as HR events across phases relative to LLJ_non-HR events,
454 which unexpectedly suggests the presences of LLJs do not invariably result in HR.
455 From the HR perspective, nearly 45.0% of HR events were associated with LLJs within
456 2 hours before onset relative to non-LLJ HR events. In general, these findings imply
457 an association between HR and LLJ in ROIs during specific phases, but certain HR
458 instances can still materialize during non-LLJ events due to other influencing factors
459 (e.g., land-sea breezes, topographic lifting, or mesoscale convective systems).

460 Furthermore, at the national scale, probability distributions of rainfall intensity
461 (Fig. 6) indicated that LLJ_HR events exhibited a distinct probability advantage in the
462 high-intensity tail ($> 2 \text{ mm}/6 \text{ min}$) compared to non-LLJ_HR events during Phases 1
463 and 3. During Phases 2 and 4, however, the distributions of the two event types were
464 similar, and LLJ_HR events even exhibited somewhat weaker rainfall. Regionally,
465 rainfall intensities within the key ROIs generally exceeded the national average,
466 particularly for LLJ_HR events. Specifically, LLJ_HR events in ROI-1 and ROI-2

Deleted: However, A a

Formatted: Font color: Auto, Complex Script Font: Bold

Deleted: were ...anged from 47.2%, 43.6%, ...33.9% to
47.2% across , and 45.5% from ...he four pP ... [27]

Deleted: 1 to Phase 4. For non-HR events, LLJ_non-HR
events accounted for approximately 37.8%. These statistics
collectively demonstrate the crucial role of LLJs in initiating
and modulating nocturnal rainfall across China. ... [28]

Formatted: English (US)

Deleted:

Formatted ... [29]

Deleted:

Formatted: Font: (Asian) SimSun, Complex Script Font:
Bold, English (US), Pattern: Clear (White)

Deleted: LLJ_HR events were more likely to produce heavier
rainfall rates $\geq 2 \text{ mm}/6 \text{ min}$ than non-LLJ_HR events during
Phases 1 and 3.

Formatted ... [30]

Deleted: LLJ_HR events generally produced heavier rainfall
at the national scale compared to non-LLJ_HR events, though
the differences were less pronounced during Phases 2 and 4.

Formatted: Font: (Asian) SimSun, Complex Script Font:
Bold, English (US), Pattern: Clear (White)

Deleted: Within the key regions, both event types showed
higher probabilities of HR than the national average,
particularly for LLJ_HR events.

527 demonstrated significantly higher probabilities of heavier rainfall (≥ 2 mm/6 min),
528 while those in ROI-4 during Phase 4 favored intensities near 0.5 and 2.8 mm/6 min.
529 Notably, despite the relatively high frequency of LLJ HR events in ROI-3 during Phase
530 3, (see the pie charts in Fig. 6), their probability of producing extreme rainfall intensities
531 was lower than that of non-LLJ HR events. This suggests that LLJs may not represent
532 the dominant mechanism for extreme rainfall in this particular region and season.

533 In summary, although LLJ HR events generally exhibit higher rainfall intensities,
534 the relatively high proportion of LLJ non-HR events suggests that the mere presences
535 of LLJs does not invariably lead to HR. Therefore, further investigating the fine-scale
536 vertical structures of LLJs preceding rainfall is crucial to distinguish the specific
537 dynamical characteristics of LLJs that lead to HR.

538 3.2 Minute-scale evolution of LLJs preceding nocturnal heavy and non-heavy 539 rainfall

540 To elucidate the contrasting precursor characteristics of LLJs that lead to nocturnal
541 rainfall of differing intensities, this section examines fine-scale vertical structure and
542 continuous evolution of LLJs within 2 hours preceding both LLJ HR and LLJ non-HR
543 events during four phases in their respective ROIs. The results revealed the distinct
544 spatiotemporal variations in vertical structure and evolutionary patterns of LLJs
545 occurred across seasonal phases.

546 During Phase1 in ROI-1, LLJ HR events exhibited a significant increase in
547 frequency starting 108 min before rainfall onset, reaching secondary peaks at -84 min
548 and -60 min, culminating in maximum frequency immediately preceding HR (Fig. 7a).
549 Meanwhile, the average wind profiles showed a rapid intensify trend from 48 min
550 before HR onset, with the jet core reaching its peak wind speed (about 12.2 m s^{-1}) and
551 its height distinctly decreased (Fig. 8a), although there is the transient weakening of jet
552 strength within 60-48 min preceding HR. These LLJs featured a bimodal vertical
553 distribution with frequent occurrence layers at 0.5-1 km and 1.5-2 km AGL. This
554 structure was characteristic of double low-level jets (DLLJs), where the coexistence of
555 the boundary layer jets (BLJs) and synoptic-system-related low-level jets (SLLJs)

Deleted: extreme

Formatted: Font: (Asian) SimSun, Complex Script Font: Bold, English (US), Pattern: Clear (White)

Deleted: although ROI-3 in Phase 3 exhibited a relatively high proportion of LLJ HR events... (see the pie charts in Fig. 6), their probability of producing heavier

Formatted ... [32]

Deleted: for

Deleted: ,

Deleted: ing

Formatted: Font color: Auto, Complex Script Font: Bold

Formatted ... [33]

Deleted: This simple statistical contrast indicates that the relationship between LLJ occurrence and nocturnal rainfall intensity is not straightforward.

Formatted ... [34]

Deleted: Although previous analyses have established the importance of LLJs in HR events, it is noteworthy that approximately 70% of LLJ occurrences were not accompanied by concurrent HR (i.e., LLJ non-HR events).

Formatted: Tab stops: Not at -3.81 cm

Formatted ... [35]

Formatted: Font color: Auto, Complex Script Font: Bold, English (US)

Deleted: .

Formatted: Font color: Auto, Complex Script Font: Bold

Deleted: while

Formatted: Font color: Auto, Complex Script Font: Bold

Formatted: Font color: Auto, Complex Script Font: Bold, English (US)

Formatted: Font color: Auto, Complex Script Font: Bold

Formatted: Font color: Auto, Complex Script Font: Bold, English (US)

Formatted ... [37]

Formatted: Font color: Auto, Complex Script Font: Bold, English (US)

Formatted: Font color: Auto, Complex Script Font: Bold

Deleted: . Wind profiles showed that LLJs strength maximized at 48 min preceding rainfall accompanied by a slight downward extension, followed by a modest weakening (Fig. 8a)... ..his observed bimodal...structure is

Formatted: Font color: Auto, Complex Script Font: Bold

603 generates a deep layer of forced ascent via BLJ-exit convergence and SLLJ-entrance
604 divergence. This dynamical coupling significantly favors organized deep convection in
605 ROI-1 (Uccellini and Johnson, 1979; Du and Chen, 2018; Du and Chen, 2019; Liu et
606 al., 2020). Note that the composite wind profile (Fig. 8a) does not show a distinct
607 bimodal vertical distribution due to smoothing from averaging. Detailed examination
608 of wind profiles revealed that approximately 40% of LLJ HR events exhibited DLLJs,
609 while only 20% of LLJ non-HR events showed such a structure. Therefore, LLJ non-
610 HR events lacked this dynamic coupling, with jets predominantly confined to the single
611 0.5–1 km layer. Although LLJ non-HR events showed a gradual increase in frequency
612 from -48 min, along with strengthening winds prior to rainfall (Figs. 7e and 8e), these
613 changes were rather limited compared to the pronounced evolution seen in LLJ HR
614 events under a background of overall lower frequency and weaker intensity. This steady
615 and weak dynamical structure failed to provide sufficient dynamic lifting to efficiently
616 initiate strong convection.

617 Both event types exhibited notably high frequencies and intensities of LLJs over
618 ROI-2 during Phase 2, yet their evolutionary dynamics diverged sharply. For LLJ HR
619 events, a coherent oscillatory vertical reorganization of LLJs is evident (Figs. 7b and
620 8b). At the first stage, both LLJ frequency and wind speed maximum peaked (exceeding
621 12 m s^{-1}) at -120 min, with the core situated 1.5–2 km AGL. Subsequently, a rapid
622 descent of frequently occurring height of LLJs to below 1 km AGL occurred,
623 accompanied by a concurrent decline in frequency and profile intensity to a minimum
624 around 84–72 min preceding HR. Analysis of wind kinetic energy and its vertical
625 transport (see Eqs. 1 and 2 in supporting material) confirmed that the ‘sudden drop’
626 likely results from the downward momentum transfer (Fig. S7a and c), which can
627 efficiently enhance low-level disturbances and dynamic forcing and serve as an
628 effective indicator of HR 1–2 hours later (Liu et al. 2003; Fu et al., 2020). Following
629 this descent, a distinct recovery phase ensued from -60 min, where the frequency
630 increased reaching a secondary peak at -48 min and jet core re-ascended to 1–2 km
631 AGL. The LLJ profile strength re-intensified to about 11.4 m s^{-1} . This rise of the jet
632 core and secondary enhancement are likely tied to cold pool-LLJ interactions and

Formatted: Font color: Auto, Complex Script Font: Bold, Not Highlight

Deleted: oes

Deleted: id

Formatted: Font color: Auto, Complex Script Font: Bold

Formatted: Font: (Asian) SimSun, Font color: Auto, English (US), Pattern: Clear (White)

Formatted: Font color: Auto, English (US)

Formatted: Font color: Auto, English (US)

Formatted: Font color: Auto, English (US)

Deleted: After examining the wind profiles, it was found

Deleted: In contrast,

Deleted: -

Deleted: ,

Deleted: against a background of overall lower frequency and weaker intensity (39)

Deleted: the total frequency and height of LLJ occurrence (40)

Deleted: n

Deleted: At -120 min,

Deleted: the frequency of LLJs peaked and strength of wind (41)

Formatted: English (US)

Formatted: English (US)

Deleted: s

Formatted: Font: (Asian) Times New Roman, Pattern: Clear

Formatted (42)

Formatted (43)

Formatted (44)

Formatted: Font: (Asian) Times New Roman, Pattern: Clear

Deleted: 5

Deleted: 2

Deleted: b

Formatted: Not Highlight

Formatted: Not Highlight

Formatted: Not Highlight

Formatted: Font: (Asian) SimSun, Pattern: Clear (White)

Deleted: -

Deleted: -

Deleted: These values then rapidly declined to a minimum (45)

Formatted: Complex Script Font: Bold, Not Highlight

Formatted: Complex Script Font: Bold, English (US)

663 intensified upward motion or latent heat release in convective clouds (further discussed
664 in Section 3.3). In conclusion, this pattern suggests an intense internal dynamical
665 adjustment process. In comparison, LLJ non-HR events lacked such low-level
666 momentum transfer signals (Fig. S7b and d) and maintained a quasi-steady state, with
667 consistent LLJs strength (near 11.8 m s^{-1}) and a preferred height range of 1–2 km AGL
668 (Fig. 8f). The LLJs frequency exhibited gradual changes, peaking weakly at 36 min
669 preceding rainfall before a subsequent rapid decrease (Fig. 7f). This pattern indicates
670 an absence of the rapid dynamical redistribution observed in LLJ non-HR events.

671 During Phase 3 in ROI-3, LLJ HR events exhibited a bimodal temporal
672 distribution in LLJ frequency, with prominent peaks at –96 min and –48 min (Fig. 7c). The
673 dominant LLJ height was centered between 1–1.5 km AGL. The wind profiles showed
674 a corresponding evolution where the maximum wind speed increased from
675 approximately 8 m s^{-1} at –120 min to a first peak about 9.5 m s^{-1} by –84 min. It then
676 reached a secondary peak near –48 min and displayed a characteristic transient
677 weakening (–48 to –24 min), after which a rapid intensification resumed until HR
678 occurred (Fig. 8c). Conversely, LLJ non-HR events were characterized by substantially
679 lower LLJs frequency (around 20%) and more diffuse structure (Fig. 7g), with wind
680 profiles showing weaker intensification preceding rainfall (Fig. 8g). Thus, the
681 pronounced, rapid change and final intensification in LLJs likely reflect a key
682 dynamical mechanism conducive to HR initiation. However, the overall weaker wind
683 profiles potentially explained the lower probability of heavier rainfall in LLJ HR
684 events over ROI-3 during Phase 3 relative to other region and phases.

685 During Phase 4 in ROI-4, LLJ HR events exhibited a distinctive two-stage
686 intensification process. The wind profiles initially strengthened rapidly starting from –
687 120 min, reaching a primary peak of approximately 12.8 m s^{-1} at –72 min (Fig. 8d),
688 coinciding with a secondary peak in LLJ frequency. Following a brief weakening (–60
689 to –48 min), a renewed and explosive intensification occurred from –48 min onwards,
690 continuing until rainfall onset. Throughout this period, the LLJ cores remained
691 concentrated between 0.5–1.5 km AGL (Fig. 7d). In sharp contrast, LLJ non-HR
692 events displayed a pattern of premature peaking followed by decay. Both frequency and

- Deleted: The rise of jet core and secondary enhancement ... [46]
- Deleted: transient but
- Deleted: And
- Deleted: culminating in a single peak
- Deleted: before
- Deleted: , followed by a rapid decrease
- Formatted: Font color: Auto, Complex Script Font: Bold
- Formatted: Font color: Auto, Complex Script Font: Bold
- Deleted: .
- Deleted: min
- Deleted: distinct
- Deleted: occurring
- Deleted: prior to rainfall
- Deleted: T
- Deleted: -
- Deleted: -
- Deleted: -
- Deleted: ,
- Formatted ... [47]
- Deleted: -
- Deleted: -
- Formatted ... [48]
- Deleted: after which both wind speed and LLJ height ... [49]
- Deleted: This rapid vertical restructuring of LLJ is li ... [50]
- Formatted ... [51]
- Deleted: a more uniform height distribution (Fig. 7g)
- Formatted: Font color: Auto, Complex Script Font: Bold
- Deleted: intensification
- Deleted: between -96 and -48 min
- Formatted: Font color: Auto, Complex Script Font: Bold
- Deleted:
- Formatted ... [52]
- Deleted: Following a brief weakening, a renewed and ... [54]
- Formatted ... [53]
- Deleted: LLJ HR events showed a rapid frequency in ... [55]
- Deleted: Conversely,

746 intensity peaked earlier at -84 min, followed by general attenuation (Fig. 7h). By -48
747 min, weakened wind profiles stabilized into a double-core structure maintaining around
748 10 m s⁻¹, with distinct jet cores near 0.8 km and 1.7 km AGL (Fig. 8h). Crucially, in
749 the LLJ_non-HR event, this premature peak and the subsequent continuous attenuation
750 of the low-level wind field resulted in a lack of sustained dynamic forcing during the
751 critical pre-rainstorm stage, failing to trigger HR.

752 Synthesizing the evolution across all phases, although a distinct transient
753 weakening of jet profiles was consistently observed, the wind profiles of LLJs
754 consistently showed a rapid increasing and height of core decreased in around the final
755 30 min before HR. We propose that this minute-scale oscillatory behavior—
756 characterized by a 'weakening-then-strengthening' or 'descent-then-ascent' pattern—
757 represents a physically consistent signature of the dynamic environment adjustment
758 essential for HR. Physically, this phenomenon is likely attributable to the momentum
759 consumption by developing convection or the flow blocking effect due to strong
760 convergence (Markowski & Richardson, 2010). Consequently, this rapid
761 reorganization and final-stage intensification of the low-level dynamical field
762 constitutes a decisive triggering mechanism for HR, standing in sharp contrast to the
763 weaker, quasi-steady evolution observed in LLJ_non-HR events.

764 Furthermore, probability distributions of LLJ strength and height within 2 hours
765 preceding rainfall were compared across key regions (Fig. 9). During Phase 1 in ROI-
766 1, the strength of LLJs in LLJ_HR events was notably stronger by 2–3 m s⁻¹ than that
767 in LLJ_non-HR events (Fig. 9a). Height distributions showed distinct bimodal peaks
768 near 0.9 km and 1.75 km AGL (Fig. 9e). The average LLJs height was generally higher
769 in LLJ_HR events, which is usually affected by the coupling of the upper-level jet
770 stream or the sea-land breeze. During Phase 2 in ROI-2, LLJ_HR events showed higher
771 probabilities of strong LLJs (17–28 m s⁻¹) compared to the dominant 13 m s⁻¹ intensity
772 in LLJ_non-HR events (Fig. 9b). Influenced by large-scale circulation patterns, both
773 event types featured LLJs centered near 1.5 km AGL (Fig. 9f), though LLJ_HR events
774 developed a secondary maximum near 0.8 km AGL due to pre-rainfall descent of the
775 jet core (Fig. 7b). Contrastingly, Figure 9c shows that LLJ_HR events were associated

Deleted: -

Deleted: LLJ_non-HR events peaked earlier at -84 min in both frequency and intensity of LLJs,

Deleted: -

Formatted: Font color: Auto, Complex Script Font: Bold

Deleted: prior to the final intensification... then the final 30 minutes before HR, both LLJ frequency and (... [56])

Formatted: Font: (Asian) SimSun, Font color: Auto, English (US), Pattern: Clear (White)

Deleted: or stabilizing trend

Formatted

(... [57])

Deleted: “

Formatted: Font: (Asian) SimSun, English (US), Pattern: Clear (White)

Deleted: ”

Deleted: “

Formatted: Font: (Asian) SimSun, English (US), Pattern: Clear (White)

Deleted: ”

Formatted: Font: (Asian) SimSun, English (US), Pattern: Clear (White)

Formatted

(... [58])

Deleted: within(120–30 min prior)eceding rainfall ...nd final-stage intensification of the low-level dynamical field within the (last 30 min) (... [59])

Deleted: is crucial for triggerin...forg...HR, (... [60])

Deleted: and contrasts sharply with

Formatted: Font: (Default) Times New Roman, (Asian) SimSun, Font color: Auto, Complex Script Font: Times New Roman, Bold, English (US)

Formatted: Font: (Default) Times New Roman, (Asian) SimSun, Font color: Auto, Complex Script Font: Times New Roman, Bold, English (US)

Formatted: Font color: Auto, Complex Script Font: Bold

Deleted: , consistent with previously documented double LLJs influences (Du and Chen, 2019)... And (... [61])

Formatted: Font color: Auto, Complex Script Font: Bold, English (US)

Deleted:

Formatted: Font color: Auto, Complex Script Font: Bold

818 with weaker jet strengths (around 11 m s^{-1}) compared to LLJ_non-HR events ($14\text{--}23$
819 m s^{-1}) in ROI-3 during Phase 3, suggesting that strong LLJs don't necessarily induce
820 HR here. The height of LLJ in LLJ_HR events mainly concentrated near 1.2 km AGL,
821 whereas in LLJ_non-HR events, it was more uniformly distributed between 0–3 km
822 AGL with a higher probability nearly 1.5 km (Fig. 9g). For Phase 4 in ROI-4, LLJs
823 strength peaked near 15 m s^{-1} in both event types, but LLJ_HR events featured stronger
824 jets reaching $25\text{--}30 \text{ m s}^{-1}$ (Fig. 9d). The LLJs height in both events peaked
825 predominantly at 0.8 km AGL, with secondary peaks at 1.5 km for LLJ_HR and 2.0 km
826 AGL for LLJ_non-HR events (Fig. 9h).

827 In summary, although different internal dynamic adjustments, including frequency,
828 occurrence height, and wind profile intensity of LLJs, preceding LLJ HR events were
829 observed, due to the different dominant mechanisms influencing rainfall in each phase,
830 our findings highlight the role of fine-scale LLJ structures and their rapid vertical
831 reorganization in modulating nocturnal rainfall intensity, offering valuable insights for
832 improving regional nocturnal HR forecasting.

833 3.3 Thermodynamic evolution associated with LLJs preceding nocturnal heavy 834 and non-heavy Rainfall

835 The section 3.2 has clarified that the fine-scale dynamic characteristics of LLJs—
836 including their temporal evolution, vertical structure, and intensity variations—play a
837 pivotal role in modulating nocturnal rainfall intensity during rainy season phases.
838 However, the influence of LLJs on rainfall generation and intensification rarely
839 operates in isolation; instead, it depends strongly on the accompanying large-scale
840 thermodynamic environment, which provides the necessary moisture supply and
841 convective instability to sustain or amplify heavy rainfall. Thus, to fully unravel the
842 mechanisms underlying the distinction between LLJ_HR and LLJ_non-HR events, it is
843 essential to complement the dynamic analysis with an in-depth examination of the
844 thermodynamic conditions associated with LLJs within the immediate pre-convective
845 environment (at 1 hour prior to nocturnal rainfall onset).

Deleted: above 1.7

Deleted: -

Deleted: And

Formatted: English (US)

Deleted: except for ROI-3 during Phase 3, LLJ_HR events exhibited significantly higher probabilities of stronger jets, most notably in ROI-2 during Phase2. LLJs height were generally lower in LLJ_HR events, except in ROI-1 during Phase1. A

Formatted: Font color: Auto, Complex Script Font: Bold

Formatted: Font color: Auto, Complex Script Font: Bold

Deleted: distinct temporal evolution patterns in frequency, occurrence height, and wind profile intensity of LLJs

Deleted: across key regions during each phase

Deleted: .

Deleted: Except for ROI-3 during Phase 3, LLJ_HR events exhibited significantly higher probabilities of stronger jets, most notably in ROI-2 during Phase2. LLJs height were generally lower in LLJ_HR events, except in ROI-1 during Phase1. Tthese

Deleted: preceding

Deleted: across different key regions and

Formatted: Font color: Auto, Complex Script Font: Bold

Deleted: in the 1-hour preceding nocturnal rainfall.

Deleted: at

Deleted: eceding

Formatted: Font color: Auto, Complex Script Font: Bold

Formatted: Font color: Auto, Complex Script Font: Bold

868 Further analysis of large-scale thermodynamic conditions at 1 hour prior to
869 nocturnal rainfall onset (Figs. 10 and 11) reveals consistently stronger thermal
870 instability for LLJ_HR versus LLJ_non-HR events, accompanied by stronger MFC
871 within key regions during each rainy season.

872 During Phase 1 in ROI-1, thermodynamic conditions were comparable between
873 event types. Southwesterly LLJs transported warm-moist air masses from the South
874 China Sea and Bay of Bengal, forming a pronounced warm-humid tongue (Fig. 10a and
875 10e). Coupled with MFC centers developing north of the jet axis (Fig. 11a and 11e),
876 this configuration facilitated nocturnal rainfall development. During Phase 2 in ROI-2,
877 LLJ_HR events exhibited a significantly stronger warm-moisture tongue with core θ_e
878 reaching 358 K—approximately 2 K higher than in non-HR events (Figs. 10b and 10f).
879 Dynamically, the stronger LLJ core ($>1.2 \text{ m s}^{-1}$ difference) drove a sharper,
880 continuous band of MFC along the left flank of the jet axis (Fig. 11b), creating a robust
881 triggering mechanism for HR (Fig. 11b). During Phase 3 in ROI-3, intensified
882 southwesterly LLJs in HR events drove substantial northward transport of abundant
883 moisture and higher θ_e air ($>2 \text{ K}$ difference) northward into a low θ_e environment (Fig.
884 10c), enhancing convective instability. The synergistic interaction of this moist, high-
885 energy advection with orographic forcing from the Taihang Mountains generated
886 intense MFC, with peak values south of Beijing approximately $30 \times 10^{-5} \text{ km m}^{-2} \text{ s}^{-1}$
887 (Fig. 11c) than those in LLJ_non-HR events, thereby driving nocturnal HR.
888 Thermodynamic contrasts were most pronounced during Phase 4 in ROI-4.
889 Thermodynamic contrasts were most pronounced during Phase 4 in ROI-4. LLJ_HR
890 events featured a deep high- θ_e region ($>356 \text{ K}$) over the southeastern Tibetan Plateau
891 (Fig. 10d), contrasting with the cold highs and lower θ_e prevalent in LLJ_non-HR
892 events (Fig. 10h). Concurrently, accelerated easterly-southeasterly LLJs drove warm,
893 moist air towards the steep eastern Plateau margin. The impingement of this flow
894 against the sharp topographic gradient generated intense dynamic lifting and low-level
895 convergence. This mechanically forced ascent, synergizing with the abundant moisture
896 transport and strong MFC (Fig. 11h), played an essential role in triggering the observed
897 nocturnal HR in this region.

Deleted: ¶

Deleted: -

Deleted: eceding

Formatted: Font color: Auto, Complex Script Font: Bold

Formatted: Font color: Auto, Complex Script Font: Bold

Formatted: Font: (Asian) SimSun, Complex Script Font: Bold, English (US), Pattern: Clear (White)

Formatted: Font: (Asian) SimSun, Complex Script Font: Bold, English (US), Pattern: Clear (White)

Formatted: Font: (Asian) SimSun, Complex Script Font: Bold, English (US), Pattern: Clear (White)

Formatted: Font: (Asian) SimSun, Complex Script Font: Bold, English (US), Pattern: Clear (White)

Formatted: Font: (Asian) SimSun, Complex Script Font: Bold, English (US), Pattern: Clear (White)

Formatted: Font: (Asian) SimSun, Complex Script Font: Bold, English (US), Pattern: Clear (White)

Formatted: Font: (Asian) SimSun, Complex Script Font: Bold, English (US), Pattern: Clear (White)

Formatted: Font: (Asian) SimSun, Complex Script Font: Bold, English (US), Pattern: Clear (White)

Deleted: although warm-moist airflow prevailed northwest of the subtropical high in both event types (Fig. 10b and 10f), LLJ_HR events exhibited more favorable thermodynamic conditions: mean θ_e was approximately 2 K higher than in LLJ_non-HR events, with a high- θ_e center reaching 358 K, alongside stronger LLJ cores ($>1.2 \text{ m s}^{-1}$ difference). Through baroclinic instability and LLJ dynamic forcing, stronger MFC centers formed along the left side of the jet axis, ultimately triggering HR

Formatted: Font: (Asian) SimSun, Complex Script Font: Bold, English (US), Pattern: Clear (White)

Deleted: LLJ_HR events were characterized by enhanced southwesterly moisture transport interacting with cold air advection from westerly troughs. Superimposed with (... [62])

Deleted:

Formatted: Font color: Auto, Complex Script Font: Bold

Formatted: Font color: Auto, Complex Script Font: Bold, English (US)

Formatted: Font color: Auto, Complex Script Font: Bold

Formatted: Font color: Auto, Complex Script Font: Bold, English (US)

Formatted: Font color: Auto, Complex Script Font: Bold

Formatted: Font color: Auto, Complex Script Font: Bold, English (US)

Deleted: Unlike LLJ_non-HR events characterized by (... [63])

931 To elucidate the rapid processes leading to occurrence of rainfall, the minute-scale
 932 evolution of key thermodynamic and dynamic parameters was further analyzed (Fig.
 933 12), including surface θ_e , LLJ index and VWS. Specifically, LLJ index is defined as the
 934 ratio of maximum wind speed below 3 km to the height where wind first exceeds 10 m
 935 s^{-1} . A rapid rise in LLJ index will reflect the extension and pulsing intensity of the LLJ,
 936 and its magnitude has been shown to be positively correlated with subsequent rainfall
 937 intensity 1-2 hour later (Liu et al., 2003). VWS is calculated as the wind speed
 938 difference between the surface and jet height divided by the jet height and is used to
 939 characterize the bulk shear from the surface to the jet layer associated with the
 940 dynamical forcing and organization of convection (Wei et al., 2014).

941 Figure 12a illustrates that during Phase 1 in ROI-1, despite the similarity in large-
 942 scale environments between LLJ_HR and LLJ non-HR events, they exhibited distinct
 943 differences in the continuous evolution of LLJ-associated thermodynamic conditions
 944 preceding rainfall onset. LLJ_HR events exhibited abrupt thermodynamic enhancement
 945 from 90 min preceding the onset of rainfall driven by rapid intensification of LLJs, with
 946 surface θ_e and VWS surging approximately 1.5 K and $0.5 s^{-1}$ respectively. Concurrently,
 947 the LLJ index surged from approximately 0.05 to 0.08, and VWS peaked sharply at 60
 948 min, signaling LLJs intensification and core descent (Figs. 7a, 8a). This rapid, minute-
 949 scale co-intensification of thermodynamic and dynamic processes serves as a critical
 950 precursor triggering HR. In contrast, LLJ non-HR events showed weaker increases of
 951 θ_e and VWS and a declining LLJ index (by about 0.02) alongside rising jet cores,
 952 reducing low-level shear and convergence efficiency, thereby diminishing overall
 953 rainfall intensity.

954 During Phase 2 in ROI-2, the thermodynamic environment displayed a distinct
 955 'weakening-reintensification' pattern (Fig. 12b), which aligns precisely with the
 956 intrinsic dynamical adjustments of the wind field presented in Fig. 8b. Initially, at 120
 957 min, concurrent peaks in the LLJ index and VWS were observed, coupled with a high
 958 surface θ_e of 348.3 K. During the subsequent transition period, a drastic elevation in the
 959 jet core height starting from 84 min caused a precipitous drop in the LLJ index. The
 960 timing of this rapid evolution suggests a transient optimal window for nocturnal rainfall

Formatted: Tab stops: Not at -3.81 cm

Deleted: ()

Deleted: 1 (...s defined as the ratio of maximum wind speed below 3 km to the height where wind first exceeds 10 ... [64]

Formatted: Font color: Auto, Complex Script Font: Bold

Deleted: 1

Formatted: Font: (Default) Times New Roman, Font color: Auto, Complex Script Font: Times New Roman, Bold, English (US)

Formatted: Font color: Auto, Complex Script Font: Bold

Deleted: and VWS (...WS is calculated as the wind speed difference between the surface and jet height divided by the jet height). ... [65]

Formatted: English (US)

Formatted: Font color: Auto, Complex Script Font: Bold

Deleted: ¶ ... [66]

Formatted: Font color: Auto, Complex Script Font: Bold

Formatted: ... [67]

Formatted: Font color: Auto, Complex Script Font: Bold

Deleted:

Deleted: by 0.03

Deleted: -

Formatted: ... [68]

Deleted: This coordinated intensification suggests a tightly coupled process in which low-level warming and moistening reinforced wind acceleration, thereby enhancing shear and promoting deeper lifting conducive to HR.

Formatted: ... [69]

Deleted: LLJ index...and VWS ... [70]

Deleted: exhibit...d a distinct 'weakening-reintensification' pattern (Fig. 12b), which aligncorrespond... precisely with to ...he inte...istic nal ...ynamical adjustments of the wind field shown...resented in Fig. 8b. Initially, at -...20 min, concurrent peaks in the LLJ index and VWS were observed, coupled with a high surface θ_e of 348.3 K. During the subsequent transition period, a drastic elevation in the jet core height starting from -- ... [71]

Deleted: ¶

During Phase 2 in ROI-2, LLJ_HR events showed concurrent peaks in dynamic parameters (LLJ index, strength and VWS) coupled with high θ_e (348.3K) at -120 min (Fig. 12b). ... [72]

1050 triggering that is characteristic of LLJ_HR events in ROI-2. Following this, rapid
 1051 surface cooling began 60 min prior to HR. This cooling was likely induced by the
 1052 outflow of cold pool outflow associated with alternation or propagation of convective
 1053 systems embedded within the Mei-Yu front cloud system (Zhang et al., 2023). The
 1054 resulting dense cold air wedging beneath the strong southwesterly LLJs can lift the jet
 1055 axis above the cold-pool interface, further enhancing uplift and promoted rainfall (Luo
 1056 et al. 2014). This in turn facilitated the final re-intensification of the jet structure (Fig.
 1057 7b and 8b). Importantly, this configuration sharply enhances low-level vertical wind
 1058 shear and horizontal convergence (Fig. 12b), further promoting HR development. For
 1059 LLJ_non-HR events, weaker thermodynamic support and diminished dynamic forcing
 1060 with consistently lower LLJ indices within 60 min preceding rainfall resulted in
 1061 insufficient lift to sustain HR. Compared with the disordered fluctuations of the
 1062 LLJ_non-HR events, these results emphasized the importance of thermal-dynamic
 1063 synergy influenced by LLJs evolution in triggering HR.

1064 During Phase 3 in ROI-3, LLJ_HR events featured prominent thermal
 1065 compensation (surface $\Delta\theta_e > 1\text{K}$, 850hPa $\Delta\theta_e > 2\text{K}$ versus non-HR events), despite
 1066 possessing generally weaker dynamical forcing compared to other phases (Fig. 12c).
 1067 Temporally, the evolution was marked by distinct pulsations: The LLJ index exhibited
 1068 a rapid rise (from ~ 0.03 to ~ 0.06) starting 84 min prior to HR onset (Fig. 12c) driven
 1069 by a surge of LLJs profiles, while VWS peaked synchronously with the maximum LLJ
 1070 frequency. Subsequently, a secondary peak in both the LLJ index and VWS was
 1071 observed between -60 and -48 min. Although the subsequent decline in wind speed
 1072 and frequency led to notable fluctuations in these parameters, a substantial
 1073 intensification of VWS (increasing by $\sim 1.5\text{ s}^{-1}$) and LLJ index occurred within the final
 1074 24 min, driven by a rapid acceleration of the LLJ wind field. This co-evolution with
 1075 rapid surface warming (increase of 0.25 K) released convective instability and
 1076 enhanced convergence (Fig. 10). Nevertheless, the overall weaker dynamical
 1077 conditions likely limited the depth and organization of convection, explaining the
 1078 reduced probability of heavier rainfall compared to other phases. In contrast, during
 1079 LLJ non-HR events, the LLJ index (~ 0.03) and θ_e vary rather gradually.

Deleted: Subsequently, the LLJ index declined sharply and a rapid surface cooling initiates beginning 60 min prior to HR likely resulted from...the outflow of cold pool outflow associated with alternation or propagation of convective systems embedded within in ...he Mei-Yu front cloud system (Zhang et al., 2023). (... [73])

Deleted: result
Deleted: The combination of the cold air and the strong southwesterly LLJs may have further enhanced uplift and promoted rainfall (Luo et al., 2014). ...or LLJ_non-HR events, weaker thermodynamic support and diminished dynamic forcing with consistently lower LLJ indices ($\Delta I \approx 0.015$) (... [74])

Formatted: English (US)
Deleted: These contrasting features results underscored...the importance of thermal-dynamic synergy influenced by LLJs evolution in triggering HR., contrasting with the disorganized fluctuations of LLJ_non-HR events (... [75])

Formatted: No widow/orphan control, Tab stops: Not at -3.81 cm
Deleted:

Deleted: weaker dynamics
Formatted: (... [76])

Formatted: (... [77])
Deleted: LLJ index progressively increased... while (... [78])

Formatted: (... [79])
Deleted: -...0 and -- (... [80])

Formatted: (... [81])
Formatted: (... [82])

Deleted: ,
Deleted: VWS peaked synchronously with LLJ frequency. Within 30 min preceding rainfall, substantial intensification of VWS by about 1.5 m s^{-1} occurred driven by a rapid (... [83])

Formatted: Font: (Default) Times New Roman, Font color: Auto, Complex Script Font: Times New Roman, Bold
Deleted: , ...nhancing...d boundary-layer ...onvergen (... [84])

Formatted: English (US)
Formatted: Font color: Auto, Complex Script Font: Bold, Pattern: Clear (White)

Deleted: θ_e
Formatted: Font: (Default) Times New Roman, Font color: Auto, Complex Script Font: Times New Roman, Bold

1152 During Phase 4 in ROI-4, under the favorably thermal environments ($\theta_e > 346$ K),
1153 LLJ HR events showed a two-stage dynamic intensification. Initially, the LLJ index
1154 surged, while the VWS and jet intensity reached synchronous secondary peaks at -72
1155 min. In the second stage, VWS increased rapidly by ~ 0.9 (Fig. 12d), and the LLJ index
1156 maintained an overall upward trend, peaking immediately prior to onset due to the
1157 surging jet. But LLJ non-HR events showed weakening trends in both dynamic and
1158 thermodynamic conditions during the final 30 min and exhibited weaker changes
1159 ($\Delta VWS < 0.45 \text{ s}^{-1}$, $\Delta \text{LLJ index} < 0.02$), reflecting an absence of the coordinated
1160 intensification necessary to initiate and sustain HR.

1161 Although the evolution paths of the thermodynamic environment vary across
1162 different phases, a universal cross-region precursor emerges; the LLJ index and VWS
1163 consistently exhibits a strengthening or stabilizing trend in the final approximately 30
1164 min preceding HR onset, operating in concert with significant low-level warming
1165 (rising θ_e). In contrast, non-HR events generally lack this culminating dynamical
1166 intensification. Overall, these results adequately showcase the sensitivity of regional
1167 HR to the fine-scale structural evolution of LLJs and their coupling with
1168 thermodynamic environments.

1170 4. Summary and concluding remarks

1171 Wind profile measurements from a nationwide network of 31 RWP during the
1172 warm seasons (April–October) of 2023–2024 were utilized to characterize the minute-
1173 scale evolution of LLJs as dynamic precursors to nocturnal rainfall across China. By
1174 systematically comparing the vertically resolved behaviors of LLJs within the 2-hour
1175 window preceding nocturnal HR and non-HR events across four distinct rainy season
1176 phases, this study elucidates the critical dynamic-thermodynamic related to LLJs
1177 distinctions governing rainfall intensity.

1178 Statistical analysis reveals that at the national scale, nocturnal rainfall accounted
1179 for nearly half of the total warm-season precipitation, with 56% of these nocturnal
1180 events exhibiting LLJ influence within the preceding 2 hours. In the key ROIs,

Deleted: And

Deleted: explosive

Deleted: stages.

Deleted: -

Deleted: The LLJ index surged and VWS 与 LLJ 风廓线同
达到次峰值 at -72 min, and from 48 min preceding rainfall
in ROI-4 during Phase 4. with 第二阶段 VWS 迅速增长了
surging 0.9 s^{-1} and LLJ index increased ~ 0.025 (Fig. 12d)
LLJ index 总体呈现增强趋势直到降水前一刻达到峰值 due
to the surge in LLJ profiles and frequency. This rapid
strengthening of the jet occurred concurrently with a gradual
rise in $\theta_e (> 346 \text{ K})$, enhancing low-level moist static energy
and supporting vigorous uplift along the windward slope. [85]

Deleted: For LLJ non-HR events,

Deleted: in the final 30 min, both dynamic and [86]

Deleted: of dynamics with marginal temporal evolution

Deleted: variation

Deleted: variation

Deleted: $VWS < 0.45 \text{ s}^{-1}$, $\Delta I < 0.02$

Formatted [87]

Formatted: Font: (Intl) Times New Roman

Formatted [88]

Deleted: ¶ [89]

Deleted: the specific dynamical pathways

Formatted [90]

Formatted [91]

Deleted: across all phases,

Formatted [92]

Formatted [93]

Formatted [94]

Formatted [95]

Formatted [96]

Deleted: ¶

Formatted [97]

Formatted: Font color: Auto, Complex Script Font: Bold

Formatted [98]

Formatted: Font: Bold, Font color: Auto

Deleted: A critical gap remains in observing the fine vertical [99]

Deleted: At the national scale,

1253 approximately 45.0% of identified HR events were associated with LLJs. Generally,
1254 these LLJ events exhibited a distinct probability advantage in producing heavier rainfall
1255 intensities compared to non-LLJ events, underscoring the strong linkage between LLJs
1256 and nocturnal HR.

1257 Pronounced differences in LLJ evolution were consistently observed between HR
1258 and non-HR events across all phases, despite regional variations in synoptic forcing.
1259 During Phase 1 in ROI-1, a bimodal vertical distribution of LLJs and their rapid
1260 thermodynamic-dynamic co-intensification starting 84 min prior to rainfall were
1261 identified as key precursors of LLJ HR events, in sharp contrast to the decoupled
1262 dynamics of LLJ non-HR events. Phase 2 (ROI-2) was characterized by a distinct
1263 oscillatory process, where HR events featured a rapid descent of the LLJ core below 1
1264 km followed by a robust rebound, distinguishing them from the quasi-steady state of
1265 LLJ non-HR cases. In Phase 3 (ROI-3), LLJ HR events exhibited significant thermal
1266 compensation and bimodal pulsations (peaks at -96 and -48 min), with a critical final-
1267 stage intensification serving as the decisive trigger. Similarly, Phase 4 (ROI-4) featured
1268 a distinctive two-stage intensification, where a rapid LLJ surge within 48 min of onset
1269 distinguished LLJ HR events from the significantly attenuated dynamical structures of
1270 LLJ non-HR events.

1271 Although the specific dynamical pathways vary across different phases, all
1272 LLJ HR events exhibit a “final-stage intensification” of the LLJs (LLJs strength, VWS
1273 and LLJ index), specifically within the 30 min preceding rainfall, in synergy with
1274 thermodynamic instability (rising θ_e). This result can confirm the universality of the
1275 final-stage low-level dynamic intensification observed in our previous analysis (Li et
1276 al., 2024) as a robust trigger for nocturnal HR across diverse monsoon regions.
1277 Crucially, however, the current work identifies a novel “preparatory adjustment” phase
1278 (30–120 minutes prior) for LLJs structure (LLJs frequency, strength and height) that
1279 was not fully resolved in the regional study. This national-scale analysis reveals that
1280 the final dynamic trigger is contingent upon this earlier synergistic coupling of minute-
1281 scale jet evolution and thermodynamic destabilization. This coupled “rapid
1282 reorganization” process constitutes the essential, nationally valid precondition for HR

Deleted: Furthermore, nocturnal HR events in ROIs during the four different phases of rainy season were identified. Statistical results revealed that approximately 45.0% of HR events were associated with LLJs, which exhibited a higher probability of producing heavier rainfall than non-LLJ HR events,

Formatted: Font color: Auto

Deleted: Pronounced differences and varying lead times were observed in vertically resolved evolution of LLJs and their thermodynamic environments when comparing LLJ HR and LLJ non-HR events.

Deleted: During Phase 1 in ROI-1, the bimodal vertical distribution of the frequent occurrence layers of LLJs and its rapid thermodynamic-dynamic co-intensification from 84 min before rainfall are key precursors to HR, in sharp con...

Formatted: Font color: Auto

Formatted: Font color: Auto, Complex Script Font: Bold

Formatted ... [101]

Formatted: Font color: Auto, Complex Script Font: Bold

Formatted ... [102]

Formatted: Font color: Auto, Complex Script Font: Bold

Formatted ... [103]

Formatted: Font color: Auto, Complex Script Font: Bold

Formatted ... [104]

Formatted: Font color: Auto, Complex Script Font: Bold

Deleted:

Formatted ... [105]

Formatted: Font color: Auto, Complex Script Font: Bold

Formatted ... [106]

Formatted ... [107]

Formatted: Font color: Auto, Complex Script Font: Bold

Formatted ... [108]

Formatted: Font color: Auto, Complex Script Font: Bold

Deleted: ¶ ... [109]

Deleted: beyond this commonality,

Deleted: reorganization

Formatted: English (US)

Formatted: Font color: Auto

Formatted: Font color: Auto

Formatted: Font color: Auto

Deleted: broader spatiotemporal

Deleted: perspective

1355 generation, contrasting with the quasi-steady evolution observed in LLJ non-HR
1356 events. This underscores that the occurrence and intensity of nocturnal rainfall are
1357 ultimately regulated by regionally specific thermo-dynamic interactions modulated by
1358 the evolution of fine vertical structure of the LLJ.

1359 This study establishes distinct dynamic-rainfall linkages associated with LLJs
1360 across different warm-season rainy periods in China. Future research should: (1)
1361 expand multi-source observations to establish dynamic thresholds for early forecasting
1362 systems of nocturnal rainfall, and (2) develop quantitative frameworks relating LLJ
1363 structural evolution to rainfall intensity, offering theoretical support for optimizing
1364 physical processes in LLJ parameterization schemes within high-resolution numerical
1365 models. Additionally, the physical mechanisms governing evolution of LLJs height or
1366 strength immediately preceding rainfall onset require further investigation.

1367 Data Availability

1368 The LLJs retrieved from the RWP network can be acquired from
1369 <https://doi.org/10.5281/zenodo.17176759> (Li and Guo, 2025). The data from the
1370 weather station are obtained from the China Meteorological Data Service Centre at
1371 <https://data.cma.cn/en>, and the original ERA5 reanalysis data used here are available
1372 from the ECMWF in Hersbach et al. (2020).

1373 Acknowledgments

1374 This work was supported by the National Natural Science Foundation of China
1375 under Grants of 42325501, the Science and Technology Supporting Project of Guizhou
1376 Province ([2023]236), and by the National Key Research and Development Program of
1377 China under grant 2024YFC3013001. Last but not least, we appreciated tremendously
1378 the constructive comments and suggestions made by the anonymous reviewers that
1379 significantly improved the quality of our manuscript.

1380 Author Contributions

1381 The study was completed with close cooperation between all authors. JG designed
1382 the research framework; NL performed the analysis and drafted the original manuscript

Deleted: ¶

Crucially, A key finding is that nocturnal LLJ-HR events universally require rapid, coupled minute-scale dynamical-intensification occurring 30-120 min preceding rainfall onset, acting in synergy with thermodynamic instability. LLJ non-HR events consistently displayed insufficient dynamic-thermodynamic coupling, reflected in stable or declining LLJ parameters....

Deleted: intensity and timing

Formatted: Font color: Auto

Deleted:

Deleted: ¶

Formatted: Font color: Auto

Formatted: Font color: Auto, Complex Script Font: Not Bold

Formatted: Font color: Auto

Formatted: Font color: Auto

Formatted: Font color: Auto

Field Code Changed

Field Code Changed

Formatted: Font color: Auto

Formatted: Font color: Auto

Formatted: Font color: Auto

Formatted: Font color: Auto

Field Code Changed

Formatted: Font color: Auto, Complex Script Font: Not Bold

Deleted:

Formatted: Indent: First line: 0.68 cm

Deleted: and 42105090,

Deleted:

Formatted: Font color: Auto, Complex Script Font: Not Bold, English (US)

Formatted: Font: Not Bold, Font color: Auto

1397 with contribution from JG; JG, XG, ZZ, YZ. JG, NT, YW, and YZ helped revise the
1398 manuscript.

Deleted: and

1399 **Completing interests**

1400 The authors declare that they have no conflict of interest.

1401

Formatted: Font color: Auto, Complex Script Font: Not Bold

References

- 1403 **References**
- 1404 Anthes, R. A., Kuo, Y. H., Benjamin, S. G., and Li, Y. F.: The evolution of the mesoscale
- 1405 environment of severe local storms: Preliminary modeling results, Mon. Weather
- 1406 Rev., 110(9), 1187-1213, doi:10.1175/1520-0493(1982)110,1187:
- 1407 TEOTME.2.0.CO;2, 1982.
- 1408 Bai, L., Chen, G., Huang, Y., and Meng, Z.: Convection initiation at a coastal rainfall
- 1409 hotspot in South China: Synoptic patterns and orographic effects, J. Geophys. Res.
- 1410 Atmos., 126(24), e2021JD034642, doi: 10.1029/2021JD034642, 2021.
- 1411 Blackadar, A. K.: Boundary layer wind maxima and their significance for the growth
- 1412 of nocturnal inversions, Bull. Am. Meteorol. Soc., 38(5), 283-290,
- 1413 doi:10.1175/1520-0477-38.5.283, 1957.
- 1414 Bonner, W. D.: Climatology of the low-level jet, Mon. Weather Rev., 96(12), 833-850.
- 1415 doi:10.1175/1520-0493(1968)096<0833:COTLLJ>2.0.CO;2, 1968.
- 1416 Cao, Q., J. Guo, C. Xue, Z. Li, H. Xu, N. Li, Y. Sun, Z. Zhang, Y. Wang, J. Chen, Y.
- 1417 Zhou, and T. Chen: Divergent Sounding-derived Precursor Pathways Enable
- 1418 Discrimination of Dry versus Wet Severe Convective Winds. Geophysical
- 1419 Research Letters, 52, e2025GL117491. <https://doi.org/10.1029/2025GL117491>,
- 1420 2025.
- 1421 Carbone, R. E., and Tuttle, J. D.: Rainfall occurrence in the US warm season: The
- 1422 diurnal cycle, J. Clim., 21(16), 4132-4146, doi:10.1175/2008JCLI2275.1, 2008.
- 1423 Chen, G., Sha, W., Iwasaki, T., and Wen, Z.: Diurnal Cycle of a Heavy Rainfall
- 1424 Corridor over East Asia, Mon. Weather Rev., 145(8), 3365-3389,
- 1425 doi:10.1175/mwr-d-16-0423.1, 2017.
- 1426 Chen, H., Zhou, T., Neale, R. B., Wu, X., and Zhang, G. J.: Performance of the new
- 1427 NCAR CAM3. 5 in East Asian summer monsoon simulations: Sensitivity to
- 1428 modifications of the convection scheme, J. Clim., 23(13), 3657-3675,
- 1429 doi:10.1175/2010JCLI3022.1, 2010.
- 1430 Chen, T., Guo, J., Guo, X., Zhang, Y., Xu, H., and Zhang, D.-L.: On the multiscale
- 1431 processes leading to an extreme gust wind event in East China: Insights from radar

1432 [wind profiler mesonet observations. Journal of Geophysical Research:](#)
1433 [Atmosphere, 129, e2024JD041484, doi: 10.1029/2024JD041484, 2024.](#)

1434 [Chen, X., F. Zhang, and K. Zhao: Diurnal Variations of the Land-Sea Breeze and Its](#)
1435 [Related Precipitation over South China. J. Atmos. Sci., 73, 4793 - 4815,](#)
1436 [doi:10.1175/JAS-D-16-0106.1, 2016.](#)

1437 [Chen, Y. L., and Li, J.: Large-scale conditions favorable for the development of heavy](#)
1438 [rainfall during TAMEX IOP 3, Mon. Weather Rev., 123\(10\), 2978-3002, 1995.](#)

1439 [China Meteorological Administration: Specification for Automatic Observation of](#)
1440 [Ground Meteorology. China Meteorological Press, 2020.](#)

1441 [Davis, C. A., Maning, W. K., Carbone, R., Trier, S., and Tuttle, J.: Coherence of warm-](#)
1442 [season continental rainfall in numerical weather prediction models, Mon. Weather](#)
1443 [Rev., 131, 2667-2679, doi:10.1175/1520-](#)
1444 [0493\(2003\)131<2667:COWCRI>2.0.CO;2, 2003.](#)

1445 [Dong, F., Zhi, X., Zhang, L., and Ye, C.: Diurnal variations of coastal boundary layer](#)
1446 [jets over the northern South China Sea and their impacts on diurnal cycle of](#)
1447 [rainfall over southern China during the early-summer rainy season, Mon. Weather](#)
1448 [Rev., 149\(10\), 3341-3363, doi:10.1175/MWR-D-20-0292.1, 2021.](#)

1449 [Doubler, D. L., Winkler, J. A., Bian, X., Walters, C. K., and Zhong, S.: An NARR-](#)
1450 [derived climatology of southerly and northerly low-level jets over North America](#)
1451 [and coastal environs, J. Appl. Meteorol. Climatol., 54\(7\), 1596-1619,](#)
1452 [doi:10.1175/JAMC-D-14-0311.1, 2015.](#)

1453 [Du, Y., and Chen, G.: Heavy Rainfall Associated with Double Low-Level Jets over](#)
1454 [Southern China. Part II: Convection Initiation, Mon. Weather Rev., 147\(2\), 543-](#)
1455 [565, doi:10.1175/mwr-d-18-0102.1, 2019.](#)

1456 [Du, Y., and G. Chen: Heavy Rainfall Associated with Double Low-Level Jets over](#)
1457 [Southern China. Part I: Ensemble-Based Analysis, Monthly Weather Review, 146,](#)
1458 [3827 - 3844, doi: 10.1175/MWR-D-18-0101.1, 2018.](#)

1459 [Du, Y., Chen, G., Han, B., Bai, L., and Li, M.: Convection initiation and growth at the](#)
1460 [coast of South China. Part II: Effects of the terrain, coastline, and cold pools, Mon.](#)
1461 [Weather Rev., 148\(9\), 3871-3892, doi:10.1175/MWR-D-20-0090.1, 2020.](#)

Deleted: -

1463 Du, Y., Zhang, Q., Ying, Y., and Yang, Y.: (2012). Characteristics of low-level jets in
1464 Shanghai during the 2008-2009 warm seasons as inferred from wind profiler radar
1465 data. J. Meteorol. Soc. Jpn. Ser. II, 90(6), 891-903, doi:10.2151/jmsj.2012-603,
1466 2012.

1467 Fu, S. M., Jin, S. L., Shen, W., Li, D. Y., Liu, B., & Sun, J. H.: A kinetic energy budget
1468 on the severe wind production that causes a serious state grid failure in Southern
1469 Xinjiang China, Atmospheric Science Letters, 21(7), e977, 2020.

1470 Gebauer, J. G., Shapiro, A., Fedorovich, E., and Klein, P.: (2018). Convection Initiation
1471 Caused by Heterogeneous Low-Level Jets over the Great Plains, Mon. Weather
1472 Rev., 146(8), 2615-2637, doi:10.1175/mwr-d-18-0002.1, 2018.

1473 Guo, J., Liu, B., Gong, W., Shi, L., Zhang, Y., Ma, Y., Zhang, J., Chen, T., Bai, K.,
1474 Stoffelen, A., de Leeuw, G., and Xu, X.: Technical note: First comparison of wind
1475 observations from ESA's satellite mission Aeolus and ground-based radar wind
1476 profiler network of China, Atmos. Chem. Phys., 21, 2945-2958, doi: 10.5194/acp-
1477 21-2945-2021, 2021 (data available at: <https://data.cma.cn>, last access: 11 January
1478 2024).

1479 Guo, X., Guo, J., Chen, T., Li, N., Zhang, F., and Sun, Y.: Revisiting the evolution of
1480 downhill thunderstorms over Beijing: a new perspective from a radar wind profiler
1481 mesonet, Atmos. Chem. Phys., 24(14), 8067-8083, doi:10.5194/acp-24-8067-
1482 2024, 2024.

1483 Guo, X., Guo, J., Zhang, D. L., and Yun, Y.: Vertical divergence profiles as detected
1484 by two wind-profiler mesonets over East China: Implications for nowcasting
1485 convective storms, Q. J. R. Meteorol. Soc., 149(754), 1629-1649,
1486 doi:10.1002/qj.4474, 2023.

1487 Hersbach, H., Bell, B., Berrisford, P., Biavati, G., Horányi, A., Muñoz Sabater, J.,
1488 Nicolas, J., Peubey, C., Radu, R., Rozum, I., Schepers, D., Simmons, A., Soci, C.,
1489 Dee, D. and Thépaut, J-N.: ERA5 hourly data on pressure levels from 1940 to
1490 present. Copernicus Climate Change Service (C3S) Climate Data Store (CDS),
1491 doi: 10.24381/cds.bd0915c6 (Accessed on 06-05-2024), 2023.

1492 Higgins, R. W., Yao, Y., Yarosh, E. S., Janowiak, J. E., and Mo, K. C.: Influence of the
1493 Great Plains low-level jet on summertime precipitation and moisture transport
1494 over the central United States, J. Clim., 10(3), 481-507, 1997.

1495 Hodges, D., and Pu, Z.: Characteristics and Variations of Low-Level Jets and
1496 Environmental Factors Associated with Summer Precipitation Extremes over the
1497 Great Plains. J. Clim., 32(16), 5123-5144, doi:10.1175/JCLI-D-18-0553.1, 2019.

1498 Holton, J. R.: The diurnal boundary layer wind oscillation above sloping terrain, Tellus,
1499 19(2), 200-205, doi: 10.3402/tellusa.v19i2.9766, 1967.

1500 Horinouchi, T., Matsumura, S., Ose, T., and Takayabu, Y. N.: Jet-precipitation relation
1501 and future change of the mei-yu-baiu rainband and subtropical jet in CMIP5
1502 coupled GCM simulations, J. Clim., 32(8), 2247-2259, doi:10.1175/JCLI-D-18-
1503 0426.1, 2019.

1504 Huang, X., Sun, J., and Liu, W.: The interaction between low-level jet evolution and
1505 severe convective rainstorms under topographic effect, Acta Meteorol. Sin., 78(4),
1506 551-567, 2020.

1507 Li, N., and Guo, J.: Data for wind profiles associated with LLJs obtained from RWP
1508 observations during the warm season (April-October) of 2023-2024 in China [Data
1509 set]. Zenodo. <https://doi.org/10.5281/zenodo.17176759>, 2025.

1510 Li, N., Guo, J., Wu, M., Zhang, F., Guo, X., Sun, Y., Zhang Z., Liang L., Chen T.: Low-
1511 level jet and its effect on the onset of summertime nocturnal rainfall in Beijing,
1512 Geophys. Res. Lett., 51, e2024GL110840, doi:10.1029/2024GL11084, 2024.

1513 Li, X., and Du, Y.: Statistical relationships between two types of heavy rainfall and
1514 low-level jets in South China, J. Clim., 34(21), 8549-8566, doi:10.1175/JCLI-D-
1515 21-0121.1, 2021.

1516 Liu, B., Ma, Y., Guo, J. and Wei, G.: Boundary layer heights as derived from ground-
1517 based radar wind profiler in Beijing, IEEE Trans. Geosci. Remote Sens., 57, 8095-
1518 8104, doi:10.1109/TGRS.2019.2918301, 2019.

1519 Liu, X., Luo, Y., Huang, L., Zhang, D. L., & Guan, Z: Roles of double low-level jets in
1520 the generation of coexisting inland and coastal heavy rainfall over south China

1521 during the presummer rainy season, Journal of Geophysical Research:
1522 Atmospheres, 125(18), e2020JD032890, 2020.

1523 Luo, Y., Gong, Y., and Zhang, D. L.: Initiation and organizational modes of an extreme-
1524 rain-producing mesoscale convective system along a mei-yu front in East China,
1525 Mon. Weather Rev., 142(1), 203-221, doi:10.1175/MWR-D-13-00111.1, 2014.

1526 Maddox, R. A.: Large-scale meteorological conditions associated with midlatitude,
1527 mesoscale convective complexes, Mon. Weather Rev., 111(7), 1475-1493, 1983.

1528 Marengo, J. A., Soares, W. R., Saulo, C., and Nicolini, M.: Climatology of the low-
1529 level jet east of the Andes as derived from the NCEP-NCAR reanalyses:
1530 Characteristics and temporal variability, J. Clim., 17(12), 2261-2280, 2004.

1531 Markowski, P., & Richardson, Y.: Mesoscale meteorology in midlatitudes, John Wiley
1532 & Sons, 2011.

1533 Miao, Y., Guo, J., Liu, S., Wei, W., Zhang, G., Lin, Y., and Zhai, P.: The Climatology
1534 of Low-Level Jet in Beijing and Guangzhou, China, J. Geophys. Res. Atmos.,
1535 123(5), 2816-2830. doi:10.1002/2017jd027321, 2018.

1536 Mitchell, M. J., Arritt, R. W., and Labas, K.: A climatology of the warm season Great
1537 Plains low-level jet using wind profiler observations, Weather Forecast., 10(3),
1538 576-591, 1995.

1539 Molod, A., Salmun, H. and Collow, A.B.M.: Annual cycle of planetary boundary layer
1540 heights estimated from wind profiler network data, J. Geophys. Res. Atmos., 124,
1541 6207-6221, doi:10.1029/2018JD030102, 2019.

1542 Monaghan, A. J., Rife, D. L., Pinto, J. O., Davis, C. A., and Hannan, J. R.: Global
1543 precipitation extremes associated with diurnally varying low-level jets, J. Clim.,
1544 23(19), 5065-5084, 2010.

1545 Pan, H., and Chen, G.: Diurnal variations of precipitation over North China regulated
1546 by the mountain-plains solenoid and boundary-layer inertial oscillation, Adv.
1547 Atmos. Sci., 36(8), 863-884, doi:10.1175/2010JCLI3515.1, 2019.

1548 Pitchford, K. L., and London, J.: The low-level jet as related to nocturnal thunderstorms
1549 over Midwest United States, J. Appl. Meteorol., 1(1), 43-47, 1962.

1550 Rasmussen, K. L., and Houze Jr, R. A.: Convective initiation near the Andes in
1551 subtropical South America, Mon. Weather Rev., 144(6), 2351-2374,
1552 doi:10.1175/MWR-D-15-0058.1, 2016.

1553 Reif, D. Q., and Bluestein, H.: A 20-year climatology of nocturnal convection initiation
1554 over the central and southern great plains during the warm season, Mon. Weather
1555 Rev., 145, 1615-1639, doi:10.1175/MWR-D-16-0340.1, 2017.

1556 Roots, M., Sullivan, J. T., and Demoz, B.: Mid-Atlantic nocturnal low-level jet
1557 characteristics: a machine learning analysis of radar wind profiles, Atmos. Meas.
1558 Tech., 18(5), 1269-1282, doi:10.5194/amt-18-1269-2025, 2025.

1559 Stensrud, D. J.: Importance of low-level jets to climate: A review, J. Clim., 1698-1711,
1560 1996.

1561 Subrahmayam, K. V., Udupa, S. R., Kumar, K. K., Ramana, M. V., Srinivasulu, J., and
1562 Bothale, R. V.: Prediction of zonal wind using machine learning algorithms:
1563 Implications to future projections of Indian monsoon jets, J. Indian Soc. Remote
1564 Sens., 52(2), 371-381, 2024.

1565 Sun, S. Q., Zhai, G. H., and Lorenzo, D. O.: The relationship between large-scale low-
1566 level jet over east asia and monsoon as well as cross-equatorial currents in
1567 summer, Acta Meteorol. Sin., 1(1), 43-50, 1986.

1568 Trier, J. W. Wilson, D. A. Ahijevych, and R. A. Sobash : Mesoscale vertical motions
1569 near nocturnal convection initiation in PECAN, Mon. Weather Rev., 145, 2919-
1570 2941, doi:10.1175/MWR-D-17-0005.1, 2017.

1571 Trier, S. B., Davis, C. A., Ahijevych, D. A., Weisman, M. L., and Bryan, G. H.:
1572 Mechanisms supporting long-lived episodes of propagating nocturnal convection
1573 within a 7-day WRF model simulation, J. Atmos. Sci., 63(10), 2437-2461, doi:
1574 10.1175/JAS3768.1, 2006.

1575 Tuttle, J. D., and Davis, C. A.: Corridors of warm season precipitation in the central
1576 United States. Mon. Weather Rev., 134(9), 2297-2317, doi:10.1175/MWR3188.1,
1577 2006.

1578 Uccellini, L. W., and D. R. Johnson: The coupling of upper and lower tropospheric jet
1579 streaks and implications for the development of severe convective storms.

1580 [Monthly Weather Review, 107, 682-703, doi: 10.1175/1520-](#)
1581 [0493\(1979\)107,0682:TCOUAL.2.0.CO;2, 1979.](#)

1582 [Walters, C. K., Winkler, J. A., Shadbolt, R. P., van Ravensway, J., and Bierly, G. D.:](#)
1583 [A long-term climatology of southerly and northerly low-level jets for the central](#)
1584 [United States, *Ann. Assoc. Am. Geogr.*, 98\(3\), 521-552, 2008.](#)

1585 [Wang, D., Zhang, Y., and Huang, A.: Climatic features of the south-westerly low-level](#)
1586 [jet over southeast China and its association with precipitation over east China,](#)
1587 [Asia-Pac. J. Atmos. Sci., 49\(3\), 259-270, doi:10.1007/s13143-013-0025-y, 2013.](#)

1588 [Wang, W. C., Gong, W., and Wei, H.: A regional model simulation of the 1991 severe](#)
1589 [precipitation event over the Yangtze-Huai River valley. Part I: Precipitation and](#)
1590 [circulation statistics, *J. Clim.*, 13\(1\), 74-92, doi:10.1175/1520-](#)
1591 [0442\(2000\)013<0074:ARMSOT>2.0.CO;2, 2000.](#)

1592 [Weckwerth, T. M., and Wakimoto, R. M.: The initiation and organization of convective](#)
1593 [cells atop a cold-air outflow boundary, *Mon. Weather Rev.*, 120\(10\), 2169–2187,](#)
1594 [doi:10.1175/1520-0493\(1992\)120,2169:TIAOOC.2.0.CO;2, 1992.](#)

1595 [Weckwerth, T. M., Hanesiak, J., Wilson, J. W., et al.: Nocturnal convection initiation](#)
1596 [during PECAN 2015, *Bull. Am. Meteorol. Soc.*, 100\(11\), 2223-2239,](#)
1597 [doi:10.1175/BAMS-D-18-0299.1, 2019.](#)

1598 [Wei, W., Zhang, H. S., and Ye, X. X.: Comparison of low-level jets along the north](#)
1599 [coast of China in summer, *J. Geophys. Res. Atmos.*, 119\(16\), 9692-9706,](#)
1600 [doi:10.1002/2014jd021476, 2014.](#)

1601 [Weisman, M. L., Trapp, R. J., Romine, G. S., Davis, C., Torn, R., Baldwin, M., Bosart,](#)
1602 [L., Brown, J., Coniglio, M., Dowell, D., Evans, A. C., Galarneau, T. J., Haggerty,](#)
1603 [J., Hock, T., Manning, K., Roebber, P., Romashkin, P., Schumacher, R., Schwartz,](#)
1604 [C. S., Sobash, R., Stensrud, D., and Trier, S. B.: The mesoscale predictability](#)
1605 [experiment \(MPLEX\), *Bull. Am. Meteorol. Soc.*, 96\(12\), 2127-2149,](#)
1606 [doi:10.1175/bams-d-13-00281.1, 2015.](#)

1607 [Whiteman, C. D., Bian, X., and Zhong, S.: Low-level jet climatology from enhanced](#)
1608 [Rawinsonde observations at a site in the southern Great Plains, *J. Appl. Meteorol.*,](#)

1609 36(10), 1363-1376, doi:10.1175/1520-
1610 0450(1997)036%3C1363:LLJCFE%3E2.0.CO;2, 1997.

1611 Xia, R., and Zhao, S.: Diagnosis and modeling of meso-scale systems of heavy rainfall
1612 in warm sector ahead of front in South China (middle part of Guangdong province)
1613 in June 2005, Chin. J. Atmos. Sci., 33(3), 2009.

1614 Xue, M., Luo, X., Zhu, K., Sun, Z., and Fei, J.: The controlling role of boundary layer
1615 inertial oscillations in Meiyu frontal precipitation and its diurnal cycles over
1616 China, J. Geophys. Res. Atmos., 123(10), 5090-5115,
1617 doi:10.1029/2018JD028368, 2018.

1618 Yan, Y., Cai, X., Wang, X., Miao, Y., and Song, Y.: Low-level jet climatology of China
1619 derived from long-term radiosonde observations, J. Geophys. Res. Atmos.,
1620 126(20), e2021JD035323, doi:10.1029/2021JD035323, 2021.

1621 Yu, R., Li, J., Chen, H., and Yuan, W.: Progress in studies of the precipitation diurnal
1622 variation over contiguous China, J. Meteorol. Res., 28(5), 877-902,
1623 doi:10.1007/s13351-014-3272-7, 2014.

1624 Zamora, R.J., Shapiro, M.A. and Doswell, C.A., III.: The diagnosis of upper
1625 tropospheric divergence and ageostrophic wind using profiler wind observations,
1626 Mon. Weather Rev., 115, 871-884, doi:10.1175/1520-0493(1987)1152.0.CO;2,
1627 1987.

1628 Zhang, F., Zhang, Q., Sun, J., and Xu, J.: Convection initiation during the Meiyu
1629 environment in the Yangtze-Huai River basin of China, J. Geophys. Res. Atmos.,
1630 128(9), e2022JD038077, doi:10.1029/2022JD038077, 2023.

1631 Zhang, M., and Meng, Z.: Warm-sector heavy rainfall in southern China and its WRF
1632 simulation evaluation: A low-level-jet perspective, Mon. Weather Rev., 147(12),
1633 4461-4480, doi:10.1175/MWR-D-19-0110.1, 2019.

1634 Zhang, Y., Xue, M., Zhu, K., and Zhou, B.: What is the main cause of diurnal variation
1635 and nocturnal peak of summer precipitation in Sichuan Basin, China? the key role
1636 of boundary layer low-level jet inertial oscillations, J. Geophys. Res. Atmos.,
1637 124(5), 2643-2664, doi:10.1029/2018jd029834, 2019.

1638 [Zhao, Y., Liao, J., Zhang, Q., Chen, J., Gong, X., Shi, Y., Shi, M., Yang, D., Fan, S.,](#)
1639 [Zhou, X., Cao, L., and Hu, K.: Development of China Ground Climate Normal](#)
1640 [Value Dataset from 1991 to 2020, Chinese Journal of Atmospheric Sciences \(in](#)
1641 [Chinese\), 48\(2\), 555–571, doi:10.3878/j.issn.1006-9895.2204.22010, 2024.](#)
1642
1643

Deleted: Anthes, R. A., Kuo, Y. H., Benjamin, S. G., and Li, Y. F.: The evolution of the mesoscale environment of severe local storms: Preliminary modeling results, *Mon. Weather Rev.*, 110(9), 1187-1213, doi:10.1175/1520-0493(1982)110,1187:TEOTME.2.0.CO;2, 1982.¶

Bai, L., Chen, G., Huang, Y., and Meng, Z.: Convection initiation at a coastal rainfall hotspot in South China: Synoptic patterns and orographic effects, *J. Geophys. Res. Atmos.*, 126(24), e2021JD034642, doi: 10.1029/2021JD034642, 2021.¶

Blackadar, A. K.: Boundary layer wind maxima and their significance for the growth of nocturnal inversions, *Bull. Am. Meteorol. Soc.*, 38(5), 283-290, doi:10.1175/1520-0477-38.5.283, 1957.¶

Bonner, W. D.: Climatology of the low-level jet, *Mon. Weather Rev.*, 96(12), 833-850. doi:10.1175/1520-0493(1968)096<0833:COTLLJ>2.0.CO;2, 1968.¶

Cao, Q., J. Guo, C. Xue, Z. Li, H. Xu, N. Li, Y. Sun, Z. Zhang, Y. Wang, J. Chen, Y. Zhou, and T. Chen: Divergent Sounding-derived Precursor Pathways Enable Discrimination of Dry versus Wet Severe Convective Winds. *Geophysical Research Letters*, 52, e2025GL117491. <https://doi.org/10.1029/2025GL117491>, 2025.¶

Carbone, R. E., and Tuttle, J. D.: Rainfall occurrence in the US warm season: The diurnal cycle, *J. Clim.*, 21(16), 4132-4146, doi:10.1175/2008JCLI2275.1, 2008.¶

Chen, T., Guo, J., Guo, X., Zhang, Y., Xu, H., and Zhang, D.-L.: On the multiscale processes leading to an extreme gust wind event in East China: Insights from radar wind profiler mesonet observations. *Journal of Geophysical Research: Atmosphere*, 129, e2024JD041484, doi: 10.1029/2024JD041484, 2024.¶

Chen, G., Sha, W., Iwasaki, T., and Wen, Z.: Diurnal Cycle of a Heavy Rainfall Corridor over East Asia, *Mon. Weather Rev.*, 145(8), 3365-3389, doi:10.1175/mwr-d-16-0423.1, 2017.¶

Chen, H., Zhou, T., Neale, R. B., Wu, X., and Zhang, G. J.: Performance of the new NCAR CAM3. 5 in East Asian summer monsoon simulations: Sensitivity to modifications of the convection scheme, *J. Clim.*, 23(13), 3657-3675, doi:10.1175/2010JCLI3022.1, 2010.¶

Chen, Y. L., and Li, J.: Large-scale conditions favorable for the development of heavy rainfall during TAMEX IOP 3, *Mon. Weather Rev.*, 123(10), 2978-3002, 1995.¶

... [110]

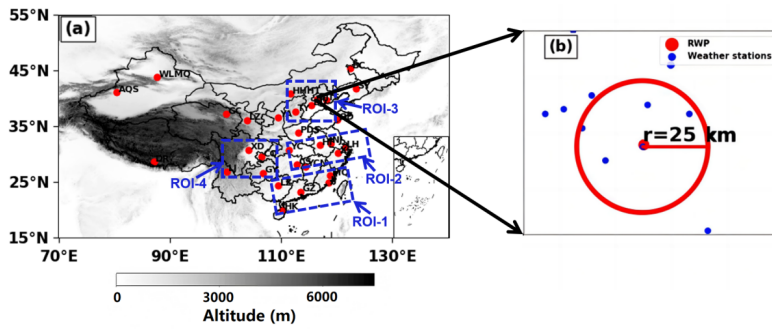
Table 1. Table of Representative Radar Wind Profiler Stations in Mainland China

Region	Station	Longitude (°)	Latitude (°)	Altitude (m)	
ROI-1	58839	MQ	118.86	26.22	160.70
	59046	LZ	109.46	24.36	314.40
	59137	JJ	118.54	24.81	124.80
	59287	GZ	113.48	23.21	65.00
	59758	HK	110.25	19.99	69.00
ROI-2	57461	YC	111.36	30.74	253.80
	57687	CS	112.79	28.11	119.00
	57793	YCN	114.36	27.79	132.00
	58238	BJ	118.90	31.93	40.60
	58321	HF	117.03	31.57	50.00
	58367	LH	121.47	31.18	5.00
	58459	XS	120.29	30.18	48.80
ROI-3	53463	HHHT	111.68	40.82	1152.10
	53772	TY	112.58	37.62	785.00
	54511	BJ	116.47	39.81	31.50
	54534	TS	118.10	39.65	23.20
	54602	BD	115.48	38.73	16.80
ROI-4	57816	GY	106.73	26.59	1197.60
	56290	XD	104.18	30.77	514.00
	56651	LJ	100.22	26.85	2382.40
Other stations	50936	BC	122.47	45.36	156.00
	51463	WLMQ	87.65	43.79	935.00
	51628	AKS	80.38	41.12	1107.10
	52754	GC	100.08	37.2	3301.50
	52889	LZ	103.89	36.06	1519.20
	57516	CQ	106.46	29.57	260.00
	53845	YA	109.45	36.58	1180.40
	54342	SY	123.51	41.73	50.00
	54857	QD	120.13	36.23	12.00
	55664	DR	87.07	28.63	4302.00
57171	PDS	113.12	33.77	142.00	

Formatted: Font: Not Bold, Complex Script Font: Bold

Formatted: Font color: Auto, Complex Script Font: Bold

1742 Figures
1743



1744
1745
1746
1747
1748
1749
1750
1751
1752
1753
1754
1755
1756
1757
1758
1759
1760
1761
1762

Figure.1 (a) Spatial distribution of 31 Radar Wind Profiler (RWP) stations across China, with four regions of interest (ROIs) demarcated by blue dashed boxes: ROI-1, ROI-2, ROI-3, and ROI-4. (b) Schematic of spatial co-location: Beijing Observatory's RWP (red circle) and rain gauges (black dots) within a 25-km radius

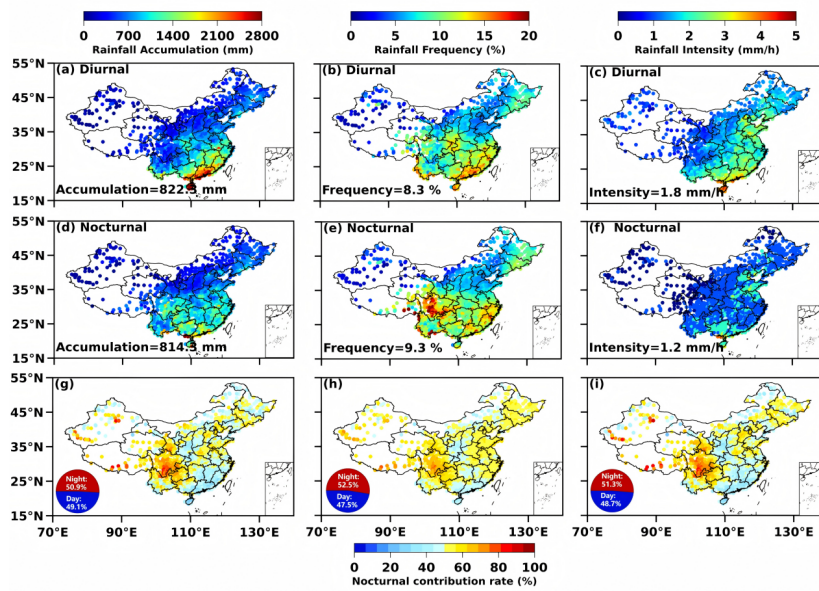
Formatted: Font: Not Bold, Font color: Auto

Formatted: Font: Not Bold, Complex Script Font: Bold

Deleted: 3

Deleted: star

Formatted: Font: Not Bold, Complex Script Font: Bold



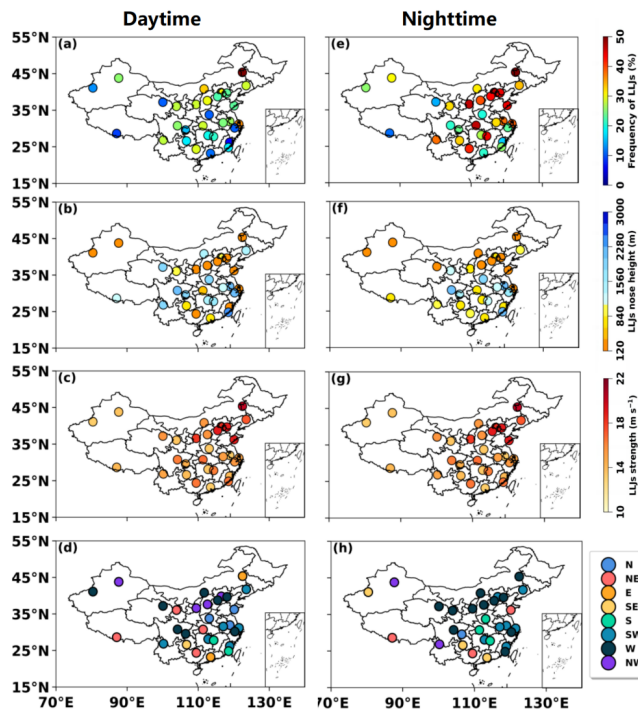
1765

1766 Figure 2. (a–c) Spatial distributions of accumulated rainfall (mm), rainfall frequency
 1767 (%), and rainfall intensity (mm/h) in the daytime from April to October in 2023–2024.
 1768 The numbers in the upper left corner represent the national average; (d–f) the same as
 1769 (a–c), but in the nighttime; (g–i) Nocturnal contribution ratios of accumulated rainfall,
 1770 frequency, and occurrence frequency of heavy rainfall (>75th percentile intensity). The
 1771 pie charts illustrate the relative contribution rates of daytime (blue) and nighttime (red)
 1772 at the national scale

1773

1774

Formatted: Font: Not Bold, Complex Script Font: Bold



1775

1776 Figure 3. (a–d) Spatial distribution of occurrence frequency, height, strength, and the
 1777 dominant wind direction of LLJs observed by 31 RWP stations during April–October
 1778 from 2023 to 2024 in the daytime. (e–h) Same as (a–d), but in the nighttime.

1779

1780

1781

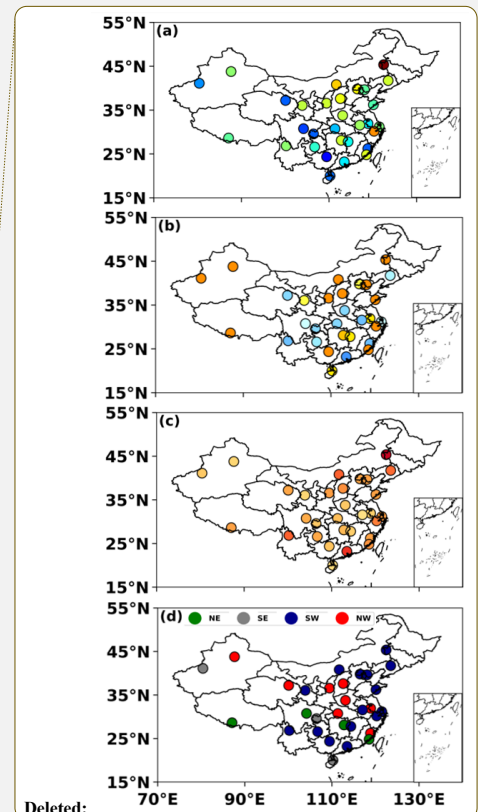
1782

1783

1784

1785

1786



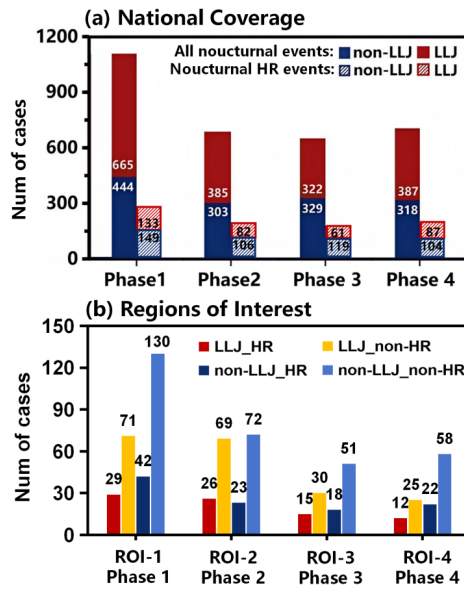
Deleted:

Formatted: Font: Not Bold, Complex Script Font: Bold

Deleted: -

Formatted: English (US)

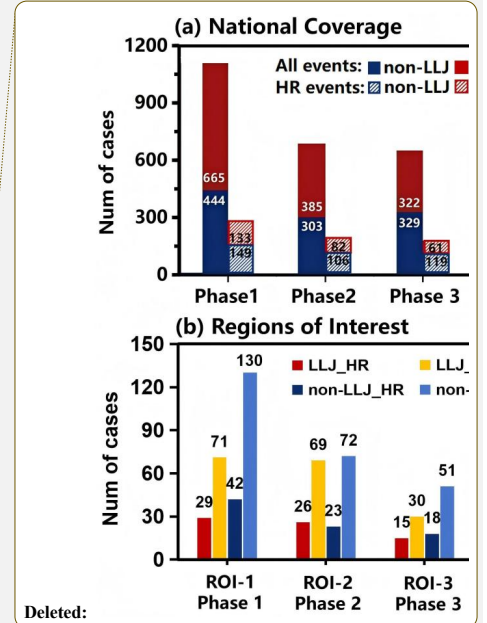
Formatted: English (US)



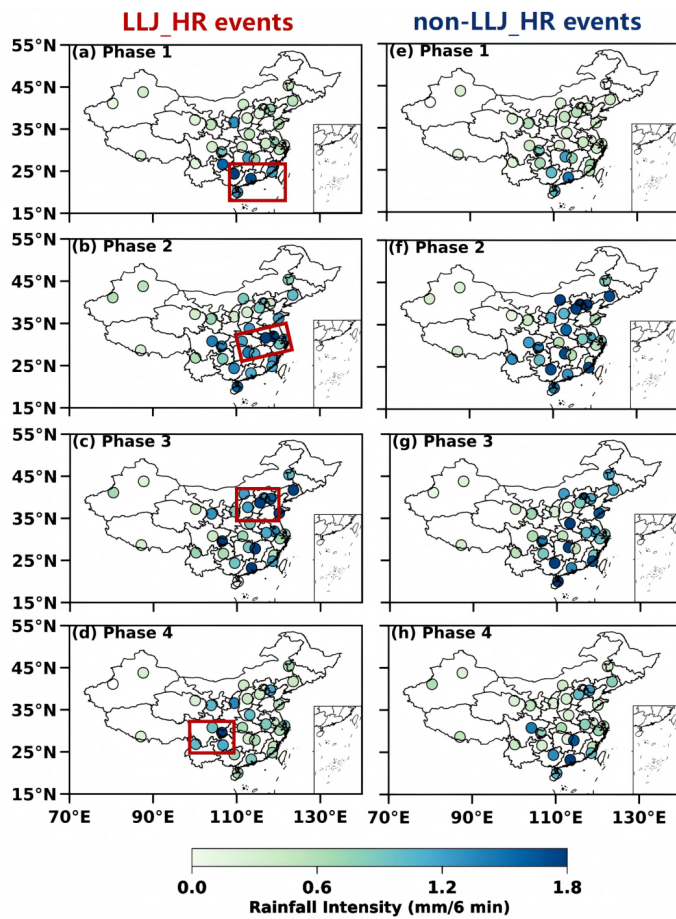
1789

1790 **Figure 4. Statistics of all nocturnal rainfall events (solid-filled bars) and heavy rainfall**
 1791 **(HR; diagonally striped bars) events across China during four phases, categorized into**
 1792 **LLJ events (red) and non-LLJ events (blue). (b) Statistics of all nocturnal events within**
 1793 **the four ROIs (ROI-1 to ROI-4) during their corresponding phases, categorized into**
 1794 **four types: LLJ HR (red), LLJ non-HR (yellow), non-LLJ HR (dark blue), and non-**
 1795 **LLJ non-HR (light blue) events.**

1796



Deleted: (a) Statistic of all nocturnal rainfall events (solid-filled bars) and heavy rainfall (HR; diagonally striped bars) events selected across China during four phases, including LLJ events (red) and non-LLJ events (blue); (b) Same as panel (a), but for nocturnal HR events in from ROI-1 to ROI-4 during corresponding phase, including LLJ-HR (red), LLJ_non-HR (yellow), non-LLJ_HR (dark blue), and non-LLJ_non-HR (light blue) events.



1806

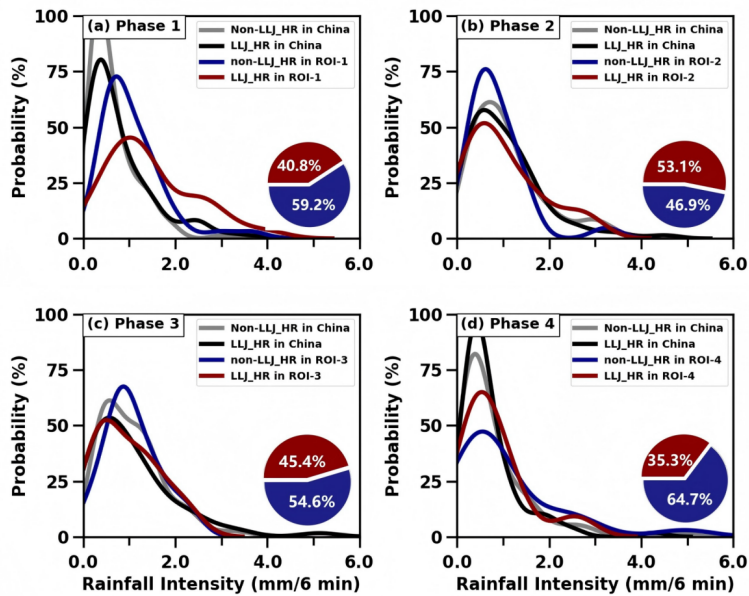
1807 Figure 5. (a-d), Spatial distributions of average rain rate (mm/6 min) for nocturnal
 1808 LLJ_HR events during the warm season from Phase 1 to Phase 4 across China; (e-h)

1809 Same as (a-d), but for non-LLJ_HR events. The red frame indicates four ROIs.

1810

Formatted: Font: Not Bold, Complex Script Font: Bold

Formatted: Font: Not Bold, Complex Script Font: Bold



1811

1812 Figure 6. (a) Probability density distributions of average rain rate (mm/6 min) for
 1813 LLJ HR events (black solid lines) and non-LLJ HR events (gray solid lines) across
 1814 China during Phase 1, and specifically in ROI-1 for LLJ HR events (red solid lines)
 1815 and non-LLJ HR events (blue solid lines). (b-d) the same as panel (a), but for
 1816 comparisons between national-scale and other regional-scale events in ROI-2 during
 1817 Phase 2, ROI-3 during Phase 3, and ROI-4 during Phase 4. The pie chart at the lower
 1818 right shows the proportion distribution of LLJ HR (red) and non-LLJ HR (blue) events
 1819 in these key regions during each period

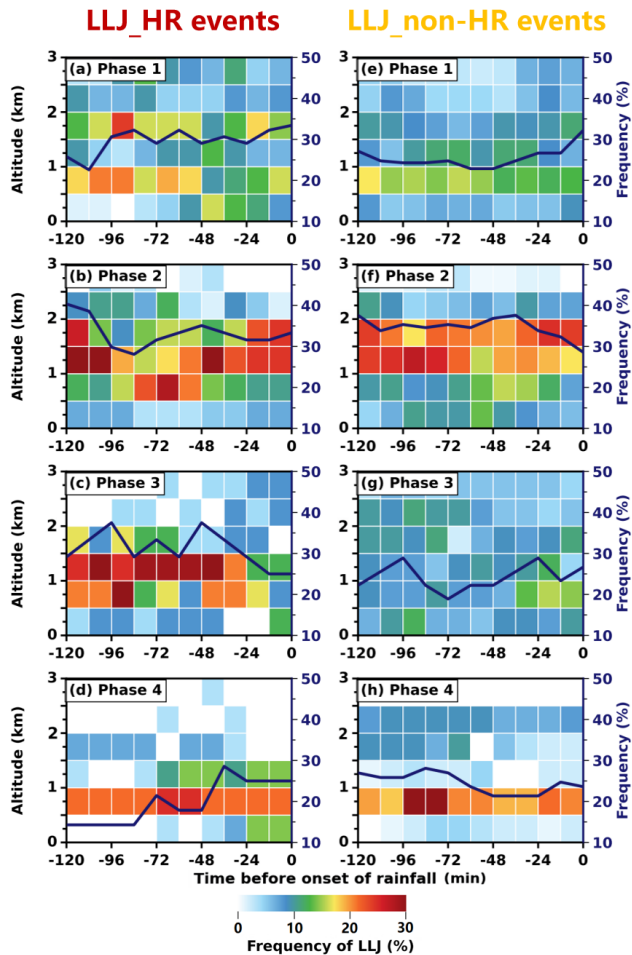
1820

Formatted: Font: Not Bold, Complex Script Font: Bold

Deleted: LLJ-HR

Deleted: LLJ-HR

Deleted: LLJ-HR



1824

1825 Figure 7. Time-height evolution of LLJ occurrence frequency (color shading, every 12
 1826 min, within 500 m vertical bins) detected by RWP with 2 hours preceding nocturnal
 1827 rainfall in LLJ_HR events in (a) ROI-1 during Phase 1, (b) ROI-2 during Phase 2, (c)
 1828 ROI-3 during Phase 3, and (d) in ROI-4 during Phase 4. Dark blue solid lines denote
 1829 accumulated LLJ frequency over 0–3 km altitude. (e-h) Same as (a-d), but for LLJ non-
 1830 HR events.

Formatted: Font: Not Bold, Complex Script Font: Bold

~~Deleted:~~ LLJ-HR

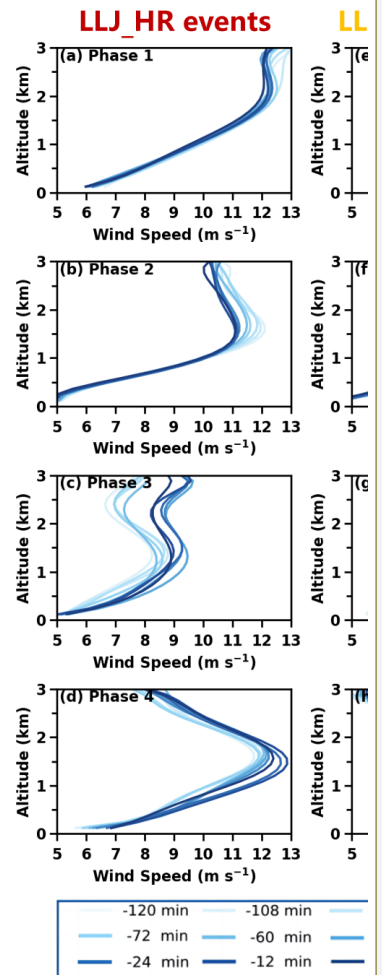
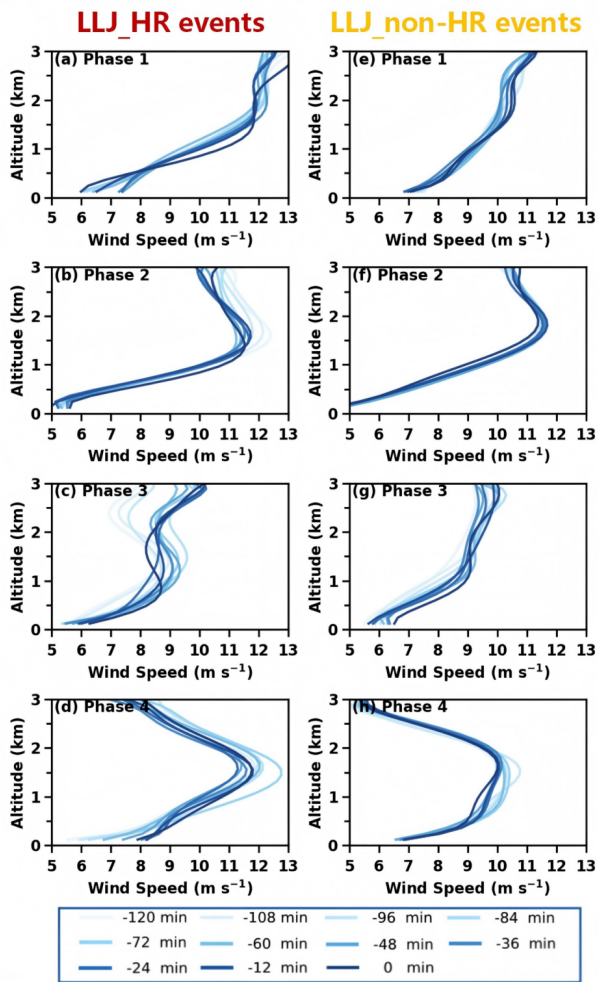
~~Deleted:~~ B

~~Deleted:~~ ack

~~Deleted:~~ for 3-km altitude

Formatted: English (US)

Formatted: Font color: Auto, Complex Script Font: Bold



Deleted:

Formatted: Font: Not Bold

Formatted: Font: Not Bold, Complex Script Font: Bold

Deleted: LLJ-HR

1835

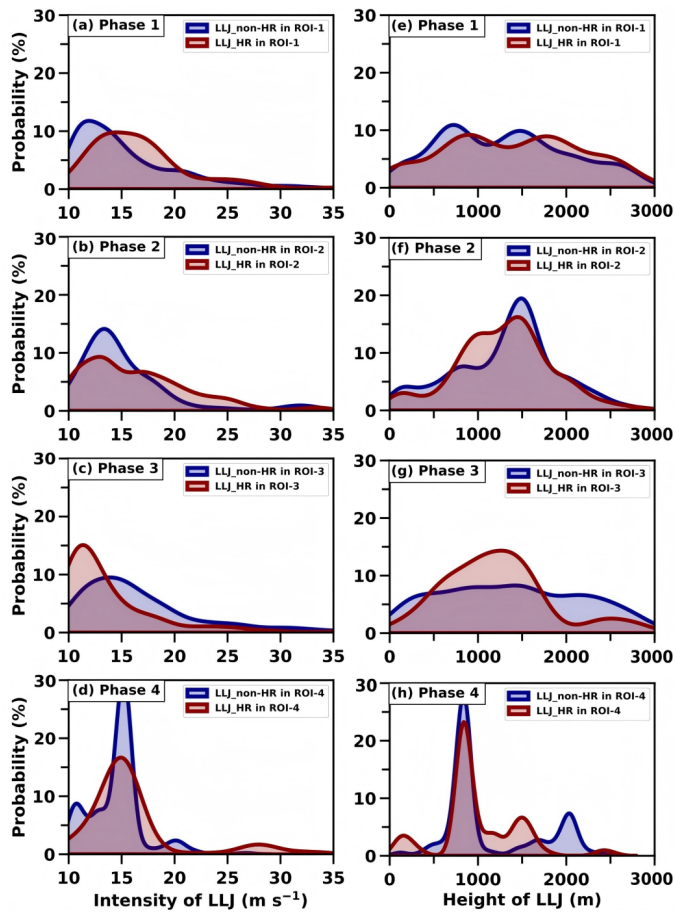
1836 Figure 8. (a-d) Evolution of RWP-detected mean wind profiles of LLJs (blue solid lines,

1837 every 12 min) within 2 hours preceding nocturnal rainfall in LLJ_HR events in (a) ROI-

1838 1 during Phase 1, (b) ROI-2 during Phase 2, (c) ROI-3 during Phase 3, and (d) in ROI-

1839 4 during Phase 4. (e-h) Same as (a-d), but for LLJ_non-HR events

1840



1843

1844

1845 Figure 9. Probability density distributions of jet core intensity from RWP observations
 1846 within 2 hours preceding nocturnal rainfall in LLJ HR events in (a) ROI-1 during Phase
 1847 1, (b) ROI-2 during Phase 2, (c) ROI-3 during Phase 3, and (d) in ROI-4 during Phase
 1848 4. (e-h) Same as (a-d), but for the height of LLJs

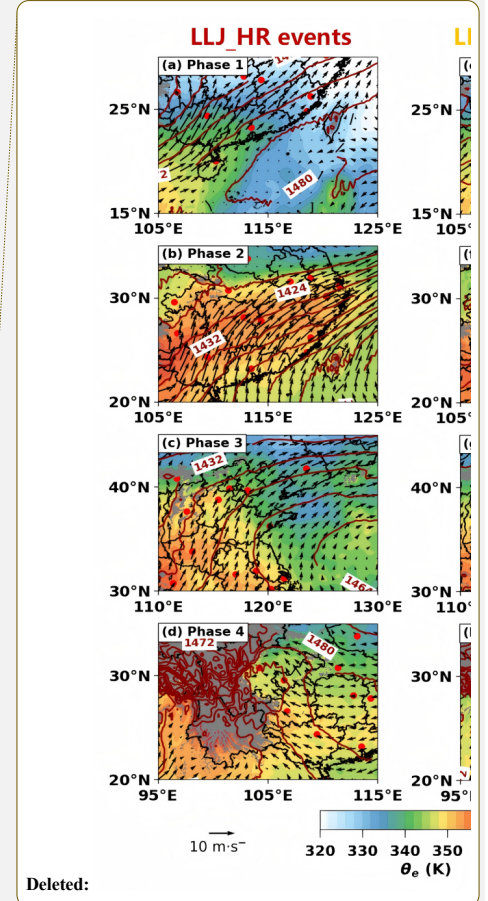
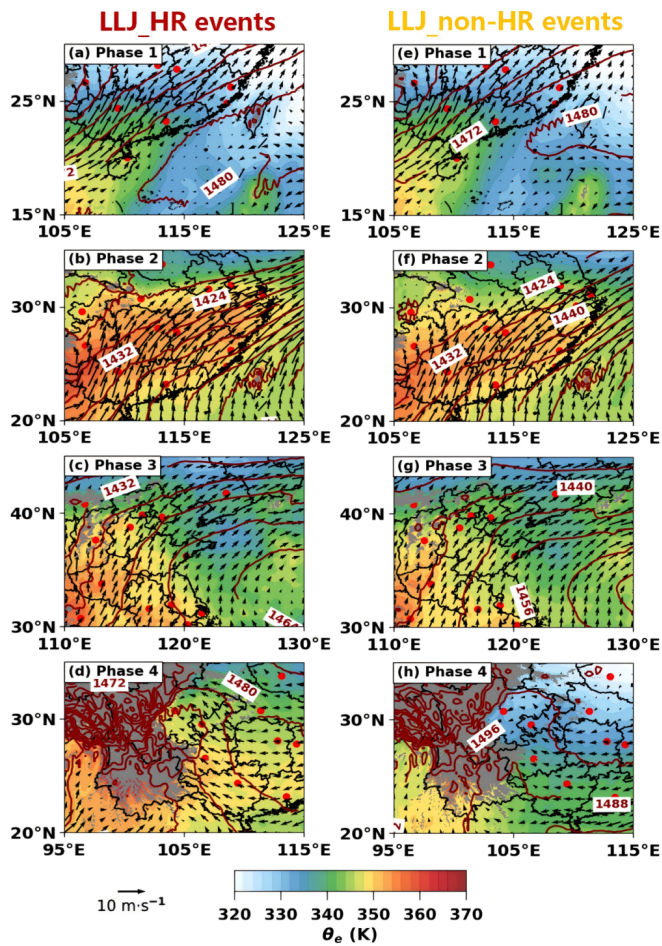
1849

1850

1851

Formatted: Font: Not Bold, Complex Script Font: Bold

Deleted: LLJ-HR



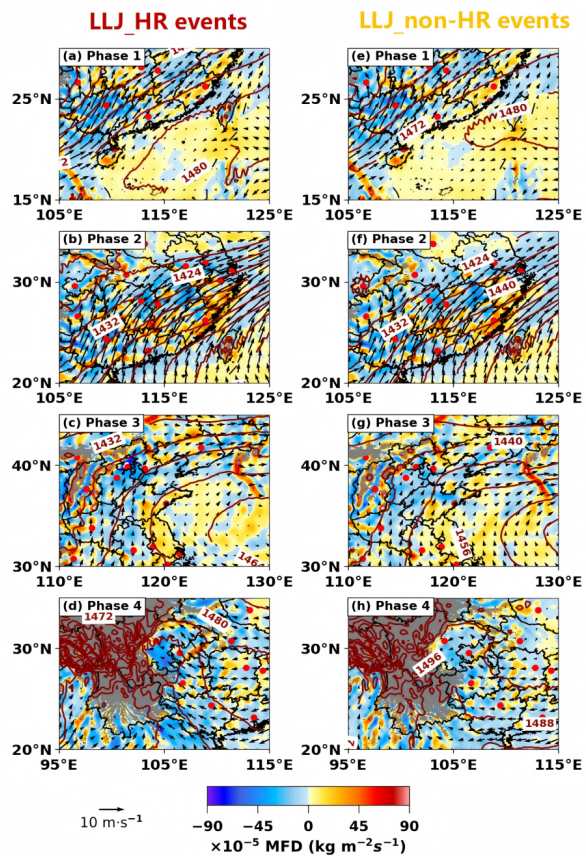
Deleted:

Formatted: Font: Not Bold, Complex Script Font: Bold

Deleted: LLJ-HR

1853

1854 Figure 10. Distributions of equivalent potential temperature (shading, unit: K) at 850
 1855 hPa, superimposed with 850 hPa horizontal wind vectors (black arrows) and
 1856 geopotential height contours (red solid lines), for LLJ HR events within 1-hour time
 1857 window preceding nocturnal rainfall onset in (a) ROI-1 during Phase 1, (b) ROI-2
 1858 during Phase 2, (c) ROI-3 during Phase 3, and (d) in ROI-4 during Phase 4. Gray
 1859 shading denotes terrain elevation exceeding 850 hPa level. The reference vector (10
 1860 m s⁻¹) is shown at the lower-left corner. (e-h) Same as (a-d), but for LLJ_non-HR events



1863

1864 Figure 11. Same as Figure 10, but showing the integrated moisture flux divergence

1865 (shading, unit: $\text{kg m}^{-2} \text{s}^{-1}$) between 1000–700 hPa at 1 hour prior to nocturnal rainfall

1866 onset

1867

1868

Formatted: Font: Not Bold, Complex Script Font: Bold

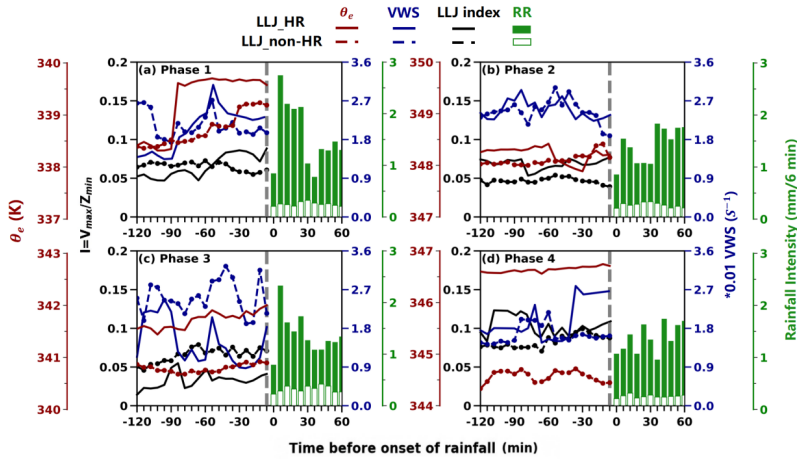
Deleted: .

Deleted:

Deleted: -

Deleted: eceding

Formatted: Font color: Auto, Complex Script Font: Bold



Formatted: Font: (Asian) SimSun, Complex Script Font: Bold

1873

1874 Figure 12. Temporal evolution of surface equivalent potential temperature (θ_e , red

Formatted: Font: Not Bold, Complex Script Font: Bold

1875 lines), vertical wind shear (VWS, blue lines), and LLJ index (I, black lines) averaged

1876 within 2 hours preceding nocturnal rainfall for LLJ HR events (solid lines) and

Deleted: LLJ-HR

1877 LLJ_non-HR events (dashed lines) in (a) ROI-1 during Phase 1, (b) ROI-2 during Phase

1878 2, (c) ROI-3 during Phase 3, and (d) in ROI-4 during Phase 4. Green bars denote 6-min

1879 averaged rain rate (mm/6 min) after LLJ HR (solid bars) and LLJ_non-HR (open bars)

Deleted: LLJ-HR

1880 events onset

1881

1882

1883

1884